ULTRAVIOLET+INFRARED STAR FORMATION RATES: HICKSON COMPACT GROUPS WITH *SWIFT* AND *SPITZER*

P. TZANAVARIS[1,2], A. E. HORNSCHEMEIER[1], S. C. GALLAGHER[3], K. E. JOHNSON[4], C. GRONWALL[5], S. IMMLER[1,6], A. E. REINES[4], E. HOVERSTEN[5], AND J. C. CHARLTON[5]

[1] Laboratory for X-ray Astrophysics, NASA/Goddard Spaceflight Center, Mail Code 662, Greenbelt, MD 20771, USA
[2] Department of Physics and Astronomy, The Johns Hopkins University, Baltimore, MD 21218, USA
[3] Department of Physics and Astronomy, The University of Western Ontario, London, ON N6A 3K7, Canada
[4] Department of Astronomy, University of Virginia, P.O. Box 400325, Charlottesville, VA 22904, USA
[5] Department of Astronomy and Astrophysics, The Pennsylvania State University, University Park, PA 16802, USA
[6] Department of Astronomy, University of Maryland, College Park, MD 20742, USA

ABSTRACT

We present *Swift* UVOT ultraviolet (UV; 1600–3000 Å) data with complete three-band UV photometry for a sample of 41 galaxies in 11 nearby (<4500 km s^{-1}) Hickson Compact Groups (HCGs) of galaxies. We use UVOT *uvw2*-band (2000 Å) photometry to estimate the dust-unobscured component, SFR$_{UV}$, of the total star formation rate, SFR$_{TOTAL}$. We use *Spitzer* MIPS 24 μm photometry to estimate SFR$_{IR}$, the component of SFR$_{TOTAL}$ that suffers dust extinction in the UV and is re-emitted in the IR. By combining the two components, we obtain SFR$_{TOTAL}$ estimates for all HCG galaxies. We obtain total stellar mass, M_*, estimates by means of Two Micron All Sky Survey K_s-band luminosities, and use them to calculate specific star formation rates, SSFR $\equiv$ SFR$_{TOTAL}/M_*$. SSFR values show a clear and significant bimodality, with a gap between low ($\lesssim 3.2 \times 10^{-11}$ yr^{-1}) and high-SSFR ($\gtrsim 1.2 \times 10^{-10}$ yr^{-1}) systems. We compare this bimodality to the previously discovered bimodality in α_{IRAC}, the MIR activity index from a power-law fit to the *Spitzer* IRAC 4.5–8 μm data for these galaxies. We find that *all* galaxies with $\alpha_{IRAC} \leqslant 0$ (> 0) are in the high- (low-) SSFR locus, as expected if high levels of star-forming activity power MIR emission from polycyclic aromatic hydrocarbon molecules and a hot dust continuum. Consistent with this finding, all elliptical/S0 galaxies are in the low-SSFR locus, while 22 out of 24 spirals/irregulars are in the high-SSFR locus, with two borderline cases. We further divide our sample into three subsamples (I, II, and III) according to decreasing H I richness of the parent galaxy group to which a galaxy belongs. Consistent with the SSFR and α_{IRAC} bimodality, 12 out of 15 type I (11 out of 12 type III) galaxies are in the high- (low-) SSFR locus, while type II galaxies span almost the full range of SSFR values. We use the *Spitzer* Infrared Nearby Galaxy Survey (SINGS) to construct a comparison subsample of galaxies that (1) match HCG galaxies in *J*-band total galaxy luminosity and (2) are not strongly interacting and largely isolated. This selection eliminates mostly low-luminosity dwarfs and galaxies with some degree of peculiarity, providing a substantially improved, quiescent control sample. Unlike HCG galaxies, galaxies in the comparison SINGS subsample are continuously distributed both in SSFR and α_{IRAC}, although they show ranges in SFR$_{TOTAL}$ values, morphologies and stellar masses similar to those for HCG systems. We test the SSFR bimodality against a number of uncertainties, and find that these can only lead to its further enhancement. Excluding galaxies belonging to HCGs with three giant galaxies (triplets) leaves both the SSFR and the α_{IRAC} bimodality completely unaffected. We interpret these results as further evidence that an environment characterized by high galaxy number densities and low galaxy velocity dispersions, such as the one found in compact groups, plays a key role in accelerating galaxy evolution by enhancing star formation processes in galaxies and favoring a fast transition to quiescence.

Key words: galaxies: interactions – galaxies: starburst – infrared: galaxies – ultraviolet: galaxies

Online-only material: color figures

1. INTRODUCTION

One of the main successes of the cold dark matter (CDM) paradigm is its prediction of hierarchical structure formation, a direct consequence of which is that galaxies are more likely to be clustered than isolated (Press & Schechter 1974; Geller & Huchra 1983). Galaxy clustering spans scales from small groups to clusters to super-clusters. Galaxy groups, including the subclass of compact groups (CGs; Rood & Struble 1994; Kelm & Focardi 2004), make up an important part of this hierarchy (Geller & Huchra 1983; Nolthenius & White 1987). Poor groups are of particular interest, as it has been established that in the nearby universe they host the majority of galaxies (see Mulchaey 2000, and references therein).

CGs are concentrations of small numbers of galaxies, which appear to occupy a compact angular area in the sky. By imposing limiting magnitude and density contrast requirements, Rose (1977) constructed the first sample of objectively selected CGs. Hickson (1982) used a different set of criteria, which included a maximum magnitude difference between four or more galaxies, limiting surface brightness, as well as an encircling ring devoid of galaxies. His catalog of 100 Hickson Compact Groups (HCGs) has been the most widely studied nearby CG sample. Sulentic (1997) re-analyzed this catalog, obtaining a revised HCG sample. In particular, this author excludes groups which contain only three spectroscopically confirmed members (triplets), as it is unclear whether such systems share the properties of groups with larger numbers of members. HCGs harbor

diverse populations of galaxies, characterized by extreme morphological variety (Mendes de Oliveira & Hickson 1994), unusual rotation curves (Rubin et al. 1991), and a high fraction of (mostly faint) active galactic nucleus (AGN; Coziol et al. 1998; Gallagher et al. 2008). CG studies have recently been extended to higher redshift (e.g., de Carvalho et al. 2005).

Thanks to the spectroscopic survey of Hickson et al. (1992), a number of key results have been established for HCGs. These authors obtained galaxy radial velocities, showing that the great majority of HCGs are not chance projections but real concentrations of galaxies: out of the full sample, 92 groups have three or more accordant members (median redshift z_{med} = 0.03). As expected for CGs, HCG member galaxies are a few galaxy radii from each other, with median projected separations of $\sim 40\,h^{-1}$ kpc. HCGs are also characterized by low velocity dispersions (radial median ~ 200 km s^{-1}), high number densities (as much as $10^8\,h^2$ Mpc^{-2}), and short crossing times (median $0.016 H_0^{-1}$). These conditions favor galaxy interactions and mergers, e.g., as observed in HCG 16 (Mendes de Oliveira et al. 1998). Further evidence for such processes is provided by an observed correlation between crossing times and the fraction of gas-rich galaxies (Hickson et al. 1992; Da Rocha et al. 2008), as well as the anticorrelation between crossing times and the fraction of intragroup light (Da Rocha et al. 2008). HCG environments are thus ideal laboratories for studying processes related to galaxy evolution and morphological transformation. In particular, HCGs, as well as CGs in general, are the only nearby environments that are closely similar to interaction environments in the earlier universe ($z \sim 4$) when galaxies were assembling hierarchically (e.g., Baron & White 1987).

The link between this highly interaction-prone environment and individual member galaxy properties remains controversial. In particular, it is unclear whether, and to what extent, star formation and/or AGN activity is either enhanced or impeded. Coziol et al. (1998) find that AGNs are mostly associated with the most luminous, early-type galaxies, as is the case in the field. However, they find that in HCGs these galaxies are preferentially located in the denser cores. They suggest an evolutionary scenario starting with merger-induced starbursts which in the case of the more massive systems evolve to become central AGN. Shimada et al. (2000) correct for the higher fraction of early-type galaxies in HCGs with respect to the field, finding no significant differences in the number of emission-line galaxies. Verdes-Montenegro et al. (1998) compare FIR and CO emission in spiral galaxies from their *IRAS* HCG sample to isolated, Virgo cluster and weakly interacting systems. They find that most HCG spirals show no enhanced FIR and CO emission, with 20% showing *reduced* CO emission. On the other hand, some early-type galaxies in HCGs are detected in CO and FIR.

Verdes-Montenegro et al. (2001) calculate the deficiency in H I in 72 HCGs. They find that HCGs with higher numbers of early-type galaxies are more deficient in H I and have a higher detection rate in the X-ray band. Using a 109-member group sample not restricted to CGs, Mulchaey et al. (2003) find evidence for diffuse X-ray emission and an intragroup medium (IGM) in half of their sample, in particular for groups containing at least one elliptical. Ponman et al. (1996) find evidence for diffuse X-ray emission in more than 75% of a sample comprising 85 HCGs.

Verdes-Montenegro et al. (2001) interpret their findings as evidence for an evolutionary sequence proceeding from H I-rich groups, (mainly containing spiral and irregular (S/I) galaxies) to H I-poor groups (mainly hosting ellipticals).

An expanded, more speculative, version of this scenario, taking into account the X-ray evidence might be as follows: initially, loose groups contract to a more compact configuration (Barton et al. 1998). At this stage, most of the H I is found in galaxy disks, which constitute the prevailing morphological type. As the effects of tidal interactions gain in importance with time, an increasing fraction of the group H I mass is stripped from the interstellar medium of member galaxies and forms tidal tails, bridges, and intergalactic structures. The atomic gas is heated and ionized at an increasing rate, filling the space between member galaxies, eventually giving rise to a hot X-ray-bright IGM that may characterize a group's final state. At this stage, groups are made up mostly of gas-poor ellipticals. As this sequence is characterized by removal of gas from individual galaxies, where it can fuel star formation, it is natural to expect a correlation between a group's H I richness and star-forming activity. Note though that this picture may still be too simplistic: in their investigation of the X-ray properties in a sample of eight highly H I-deficient HCGs, Rasmussen et al. (2008) find that only four groups have an IGM detectable in the X-rays.

Recent results in the IR provide further support to this scenario. Until recently results in this wavelength regime relied on low-sensitivity and/or angular resolution data (e.g., Allam et al. 1995; Verdes-Montenegro et al. 1998). However, Johnson et al. (2007, hereafter J07) were the first to present results on a set of 45 galaxies belonging to a sample of 12 nearby HCGs observed with *Spitzer* (IRAC and MIPS) and Two Micron All Sky Survey (2MASS). They establish trends connecting group H I-gas deficiency and the level of active star formation, implied by IR colors of individual member galaxies. They detect a "gap" in IR color–color space between gas-rich and gas-poor groups, suggestive of rapid evolution in galaxy properties. Using the same HCG sample (hereafter JG sample), Gallagher et al. (2008, hereafter G08) find further evidence for this gap in the distribution of α_{IRAC}, the mid-IR (MIR) activity index (see Section 3.1) for the nuclei of galaxies in the same HCG sample. Their findings strongly suggest a connection between α_{IRAC}, $24\,\mu$m activity, and H I content.

In this paper, we further explore the connection between group gas content, galaxy morphology, and star formation by obtaining star formation rate (SFR) and specific SFR (SSFR) estimates for 41 galaxies in the JG sample. Although it is common to use single-band data, such as UV, Hα or $24\,\mu$m to obtain such estimates (but see Kennicutt et al. 2009), these usually require corrections due to the effects of dust, which, in general, are difficult to quantify. In this respect, the UV and IR wavelength regions are complementary, and we combine information from both to obtain total SFRs consisting of a UV and an IR component.

This paper makes part of a collaborative, multi-wavelength campaign to observe and characterize the JG sample in several wavelength bands, from the X-rays to the far-IR and radio. Our main goal is to investigate whether, and to what extent, the UV regime provides support to the evolutionary scenario suggested by the IR work.

The structure of the paper is as follows. In Section 2, we give details on sample selection, UV and IR data analysis, as well as issues related to flux calculations in the UV. UV and IR results, including SFRs and SSFRs, are presented in Section 3. Section 4 discusses results and relevant uncertainties. We summarize and conclude in Section 5. We use $\Omega_M = 0.3$, $\Omega_\Lambda = 0.7$, and $H_0 = 70$ km s^{-1} Mpc^{-1} throughout.

Table 1
HCG Sample

HCG ID	$\bar{v}^{\mathrm{a}}$ (km s^{-1})	E/S0	Morphology$^{\mathrm{b}}$ S	Other	log $M_{\mathrm{H\,I}}{}^{\mathrm{c}}$ ($M_{\odot}$)	Evolutionary Stage$^{\mathrm{d}}$	H I Type$^{\mathrm{e}}$	Triplet?$^{\mathrm{f}}$
(1)	(2)	(3)	(4)	(5)	(6)	(7)	(8)	(9)
02	4309	0	2	1	10.53	Early	I	Y
07	4233	0	4	0	9.68	Early	II	N
16	3957	0	2	2	10.42	Int	I	N
19	4245	1	1	1	9.31	Early/int	II	Y
22	2686	1	2	0	9.13	Early	II	Y
31	4094	0	2	5	10.35	Int	I	N
42	3976	4	0	0	9.40	Late	III	N
48	3162	2	2(0)$^{\mathrm{g}}$	0	8.52	Late	III	N
59	4058	1	2	1	9.49	Early/int	II	N
61	3907	2	1	0	9.96	Early/int	I	Y
62	4122	4	0	0	9.06	Late	III	N

Notes.
$^{\mathrm{a}}$ Mean recession velocity for all known group member galaxies calculated from Hickson et al. (1992).
$^{\mathrm{b}}$ Taken from Hickson et al. (1989).
$^{\mathrm{c}}$ Mass of neutral hydrogen from Verdes-Montenegro et al. (2001).
$^{\mathrm{d}}$ Qualitative determination of group evolutionary stage from G08 as early, early/intermediate, intermediate, or late. This is motivated by the evolutionary scenario proposed by Verdes-Montenegro et al. (2001) and takes into account member galaxy morphology, H I deficiency, and the presence of an X-ray intragroup medium.
$^{\mathrm{e}}$ H I type as measured and defined by J07. (I) H I rich (log $M_{\mathrm{H\,I}}$/log M_{dyn} > 0.9); (II) intermediate (log $M_{\mathrm{H\,I}}$/log M_{dyn} = 0.8–0.9); and (III) H I poor (log $M_{\mathrm{H\,I}}$/log M_{dyn} < 0.8).
$^{\mathrm{f}}$ Y if group is a triplet, N otherwise.
$^{\mathrm{g}}$ Galaxies 48b and c have somewhat discordant velocities.

2. OBSERVATIONS AND DATA ANALYSIS

2.1. HCG Sample Selection

The JG sample was chosen from the original HCG catalog (Hickson et al. 1992) by application of criteria based on membership (a minimum of three giant galaxies with accordant redshifts, i.e., within 1000 km s^{-1} of the group mean), distance ($\lesssim$4500 km s^{-1}), and angular extent ($\lesssim$8′ in diameter). The analysis in the present paper does not include HCG 90, as explained in Sections 2.2 and 2.3.

Note that a sample based on these criteria includes triplets, and these are indicated in Table 1. There is some evidence that triplets may be different as a class compared to groups with four or more members: they do not show significant H I deficiency (Verdes-Montenegro et al. 2001) and their galaxies show larger velocity dispersions (Sulentic 2000), making it more likely that they are unbound systems (Sulentic et al. 2001). Indeed the original HCG catalog criteria did not include triplets, and the revised catalog of Sulentic (1997) excludes triplets altogether. We chose to keep triplets in our samples for several reasons. We are engaged on a long-term spectroscopic campaign to identify new, fainter members in our HCG galaxies. New members will affect the overall dynamics, which remains an open question. The dark matter mass also plays a role, but it is difficult to measure without more members. Further, there is no consensus that triplets should be excluded. Indeed, Sulentic (2000) argue for HCG 92 that it is possible that three of its bright galaxies make up a stable core, with the *fourth* causing it to be unstable. Tovmassian et al. (1999) specifically address the issue of reality of CGs, including triplets which are not considered to be a special case. Barton et al. (1998) include several triplets in their redshift survey of CGs, and Da Rocha & Mendes de Oliveira (2005) include a triple, HCG 95, in their investigation. We similarly prefer to simply consider triplets as one extreme of groups of galaxies. Given that CGs are relatively rare, this keeps restrictions at a minimum. In any case, including triplets does not affect the main results of this paper (see Section 4.2).

In Table 1, we present the group mean recession velocities, the member galaxy morphology, H I mass, qualitative evolutionary stage based on the Verdes-Montenegro et al. (2001) scenario, and H I-richness type from J07. H I richness is defined as the ratio log $M_{\mathrm{H\,I}}$/log M_{dyn}, where $M_{\mathrm{H\,I}}$ is the H I mass and M_{dyn} the dynamical mass, as described in J07. H I type I groups (gas rich) have log $M_{\mathrm{H\,I}}$/log M_{dyn} > 0.9; H I type II (intermediate gas rich) have log $M_{\mathrm{H\,I}}$/log M_{dyn} = 0.8–0.9; H I type III (gas poor) have log $M_{\mathrm{H\,I}}$/log M_{dyn} < 0.8.

2.2. UV Data

All galaxy groups in our HCG sample have UV data obtained with the *Swift* UV/Optical telescope (UVOT). UVOT (Roming et al. 2005), is one of three telescopes on board NASA's international *Swift* mission (Gehrels et al. 2004). The mission's primary goal is detection and characterization of gamma-ray bursts.

UVOT has a 17′ × 17′ field of view and six broadband filters covering the 1600–8000 Å range with a spatial resolution of ∼2″.5 (point-spread function (PSF) FWHM^7). Our data have been taken with the three UV filters and the bluest optical filter, *u*. The characteristics of these filters are given in Table 2.

An observation log for our *Swift* UVOT data is given in Table 3. Our targets were observed between 2006 August and 2007 November as part of a *Swift* team fill-in program (PI: C. Gronwall). The nominal exposure times were 4000 s in *uvw2*, 3000 s in *uvm2*, 2000 s in *uvw1*, and 1000 s in *u*. However, because of the nature of the fill-in program for *Swift* observations, sometimes the nominal exposure times were not matched exactly.

The data were reduced using dedicated UVOT pipeline tasks which form part of the HEASOFT package. UVOT

---
^{7} http://heasarc.gsfc.nasa.gov/docs/swift/analysis/uvot_digest.html

Table 2
UVOT and *GALEX* Bands

Filter	λ_{eff}[a] (Å)	Width[b] (Å)
UVOT[c]		
u	3501	785
uvw1	2634	693
uvm2	2231	498
uvw2	2030	657
GALEX[d]		
NUV	2271	1771–2831
FUV	1528	1344–1786

Notes.
[a] Filter effective wavelength.
[b] Widths for *GALEX* are bandpasses, and for UVOT full width at half maximum values.
[c] Data taken from Poole et al. (2008).
[d] Data taken from Morrissey et al. (2005).

sky images were prepared from raw images and event files, (task `uvotimage`) and aspect corrected (`uvotskycorr`). Final images and exposure maps were produced by combination of distinct exposures for the same observation (`uvotimsum`). Three-color composites of HCG UVOT images are shown in Figures 1–6. Note that galaxies HCG 90 B, C, and D fall on the edges of the UVOT stacked image for this HCG. This causes different parts of the same galaxy to have different exposure times and total counts. In this case, calculating total count rates is not straightforward. As HCG 90 is also not detected in the 24 μm band (see Section 2.3), all of the HCG 90 galaxies are excluded from the analysis in this paper.

For five HCGs in our sample, *Galaxy Evolution Explorer* (*GALEX*) guest investigator data (PI: J. Paramo) are also available. *GALEX* is a small-size NASA mission, with a UV telescope providing images in both a far-UV (1528 Å) and near-UV (2271 Å) band. Filter characteristics for *GALEX* are listed in Table 2. *GALEX* has a circular field of view of 1°.2 in diameter and a resolution of $\sim 6''$ (PSF FWHM; Morrissey et al. 2005). In comparison, UVOT has better spatial and color resolution, but *GALEX* can probe deeper in the FUV region both in terms of range and in terms of effective wavelength, and has higher sensitivity. We compare the *GALEX* and UVOT data in order to perform a "sanity check" for ultraviolet flux estimates (Section 2.5).

2.3. IR Data

We make use of the *Spitzer* (IRAC (3.6–8.0 μm) and MIPS (24 μm)) and 2MASS (*J*, K_s) data presented in J07. For details on the IR observations and data reduction, we refer the reader to that paper and references therein. The data are incomplete for HCG 31 F, which is too faint to be detected in the 2MASS K_s band, and HCG 90 A, which is outside the MIPS field of view. We only perform part of the analysis for 31 F. HCG 90 is excluded from our sample.

2.4. Source Detections

The photometric properties of our HCG galaxies in the near-to-mid-IR were explored in detail by J07. For consistency with that work, we obtained count rates in the same apertures used by these authors. J07 defined apertures by determining contour levels of 1.5σ–2σ on wavelength-weighted, combined

IRAC images. As these images were convolved to the MIPS 24 μm PSF, we also convolved our UVOT images to the 24 μm PSF, which is significantly broader (FWHM $\sim$ 6$''$; e.g., Dole et al. 2006, versus $\sim 2''.5$ for UVOT). Photometry on all UV images, was carried out using SURPHOT, a set of routines written specifically to allow simultaneous, net-counts-in-regions calculations on several images (Reines et al. 2008). We also reproduced the 24 μm results of J07 to ensure use of the same apertures for the UV and IR data sets. We used the same background annuli with inner and outer sizes 2 and 2.5 times the size of the apertures. We note that differences in background values obtained using these annular regions and random, source-free, regions in the same image are insignificant ($\lesssim 2\%$).

2.5. GALEX and UVOT Fluxes

UVOT and *GALEX* flux densities for our HCG sample are given in Table 4. These were obtained by multiplying measured count rates by the instrument-specific flux conversion factors given in Table 5. These were taken from Poole et al. (2008) for UVOT and the *GALEX* Web site for *GALEX*.[8] The data were corrected for Galactic extinction, using the maps of Schlegel et al. (1998) and the extinction curve of Cardelli et al. (1989). For those groups with both *GALEX* and UVOT data, we compare the UVOT *uvm2* ($\lambda_{\mathrm{eff}} = 2231$ Å) and *GALEX* NUV ($\lambda_{\mathrm{eff}} = 2271$ Å) measured fluxes, as these two filters are closest both in effective and central wavelength.

In Figure 7, we plot the fractional difference in flux between the two filters, $\Delta f_\lambda(uvm2 - \mathrm{NUV})/f_\lambda(\mathrm{NUV}))$, against *uvm2* flux. On average, the points appear to be distributed around zero, with the exception of two prominent outliers (shown as diamonds in Figure 7). The topmost one (HCG 31 F) lies close to a bright, saturated star. Because of *GALEX*'s lower resolution, part of this emission inevitably leads to an overestimate of the background for HCG 31 F in the *GALEX* image, and thus an overestimate of the *uvm2*−NUV flux difference. Otherwise, the differences are likely due to the differences in shape between the two response functions. In spite of the similarity both in effective and central wavelength, the NUV filter is more sensitive to radiation from longer wavelengths. For instance, the outlier at the bottom left of the plot (HCG 42 D) is a faint, early-type system. The redder color of this system likely leads to a higher flux estimate in the NUV filter. In fact, 4 out of 5 galaxies for which $\Delta f_\lambda(uvm2 - \mathrm{NUV})/f_\lambda(\mathrm{NUV}) < 0$ are E/S0's, and 12 out of 14 galaxies for which $\Delta f_\lambda(uvm2 - \mathrm{NUV})/f_\lambda(\mathrm{NUV}) > 0$ are S/I's.

If we exclude the two most extreme outliers, we obtain a mean fractional difference 0.03 ± 0.11. Although no general statements can be made from such a small sample (19 sources), this comparison, taken at face value, supports the publicly available flux conversion factors for *Swift* and *GALEX*. Further, this comparison provides some evidence that "coincidence loss" (see Section 2.6) is not a major concern for *uvm2*, even in cases of fairly bright sources. As explained in Section 2.6, three sources, indicated by stars in Figure 7, namely, HCG 2 B, 31 G, and 31 ACE, may suffer from this effect, with HCG 31 ACE being the brightest and most likely to be affected. If there were significant coincidence losses for these in the *uvm2* filter, NUV flux densities should be systematically higher, which is clearly not the case.

---

[8] http://galexgi.gsfc.nasa.gov/docs/galex/FAQ/counts_background.html

Table 3
Observation Log for *Swift* UVOT HCG Data (PI: C. Gronwall)

HCG ID	Observation IDs	Dates	Total Exposure Time			
			uvw2 (s)	*uvm2* (s)	*uvw1* (s)	*u* (s)
(1)	(2)	(3)	(4)	(5)	(6)	(7)
2	00035906001 00035906002	2007 Feb 11, 2007 Feb 12 2007 Nov 1	2449	2431	1623	811
7	00035907001 00035907002 00035907003 00035907004	2006 Oct 28, 2006 Oct 30 2006 Nov 10 2007 Jan 29 2007 Feb 10, 2007 Feb 11	4236	4633	2867	1406
16	00035908001 00035908002 00035908003	2006 Nov 3 2007 Feb 24 2007 Dec 3	4652	3894	2596	1292
19	00035909001 00035909002	2006 Aug 19, 2006 Aug 20 2006 Oct 30	2613	3044	2026	1012
22	00035910001 00035910002 00035910003	2006 Oct 30 2007 Mar 4, 2007 Mar 5 2007 Mar 17	4304	3798	2524	1268
31	00035911001	2006 Aug 20, 2006 Aug 21	3486	3222	2138	1066
42	00035912001 00035912002	2007 Jan 30 2007 Feb 1	3326	3027	2017	1003
48	00035913001 00035913002	2006 Nov 12, 2006 Nov 13 2006 Dec 29, 2006 Dec 30	5478	4665	3145	1560
59	00035914001 00035914002 00035914004 00035914005	2006 Nov 19 2006 Nov 22 2007 Jan 5 2007 Jun 24	2346	1755	1399	700
61	00035915001 00035915002 00035915003 00035915004	2007 Jan 30 2007 Feb 26 2007 Mar 27 2007 Mar 29	3037	3387	2162	1078
62	00035916001 00035916003 00035916004	2006 Aug 18 2006 Dec 31 2007 Jan 7	2656	4225	1727	807
90	00053602001 00035917001	2007 Apr 24 2007 Apr 27	8601	7946	6663	963

Notes. Observational data are separated according to group HCG ID (Column 1). In all cases, there are several observation IDs corresponding to a given HCG ID. Observation IDs (Column 2) and corresponding observing dates (Column 3) appear on the same row. Exposure times in each filter (Columns 4–7) are totals for each HCG.
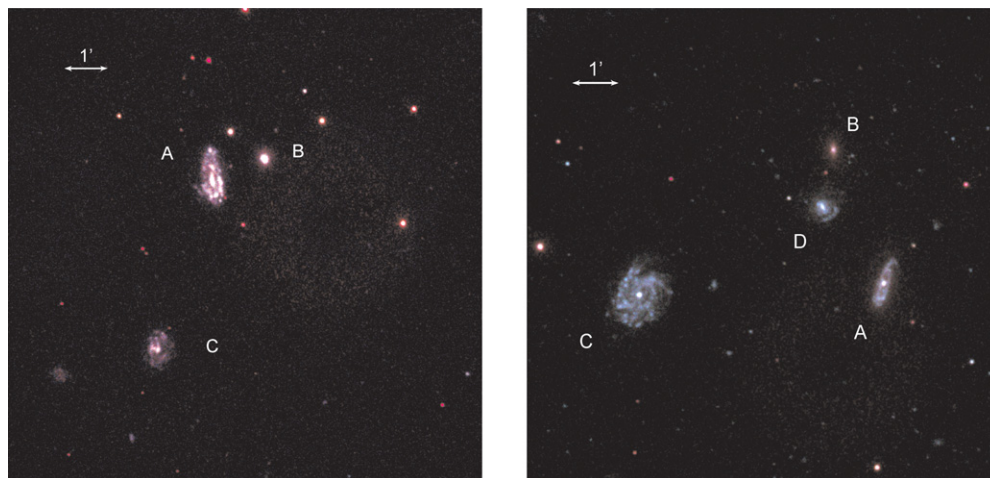

Figure 1. *Swift*/UVOT three-band images of Hickson Compact Groups (HCGs) in this sample. Blue, green, and red colors correspond to the *uvw1*, *uvm2*, and *uvw2* filters, respectively. Left: HCG 2. Right: HCG 7.
(A color version of this figure is available in the online journal.)
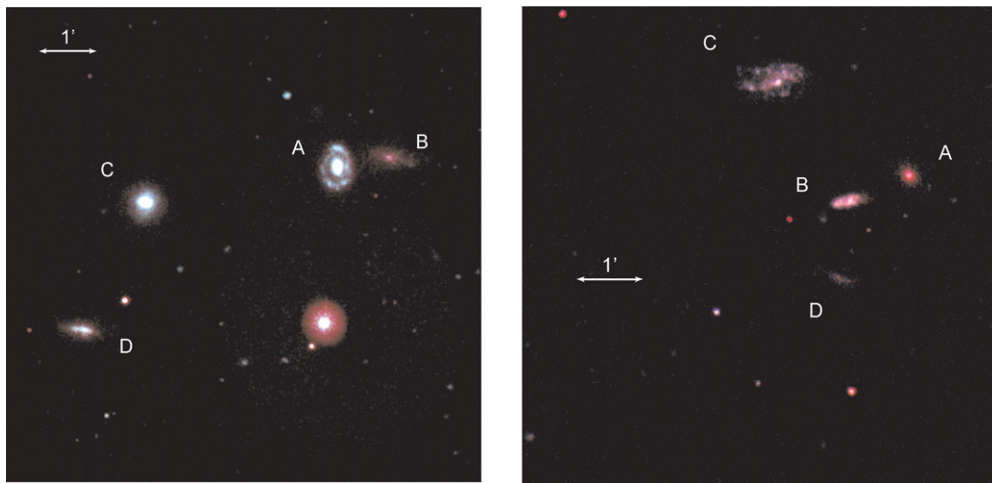
Figure 2. *Swift*/UVOT color images as in Figure 1. Left: HCG 16. Right: HCG 19. Galaxy D is a background object.
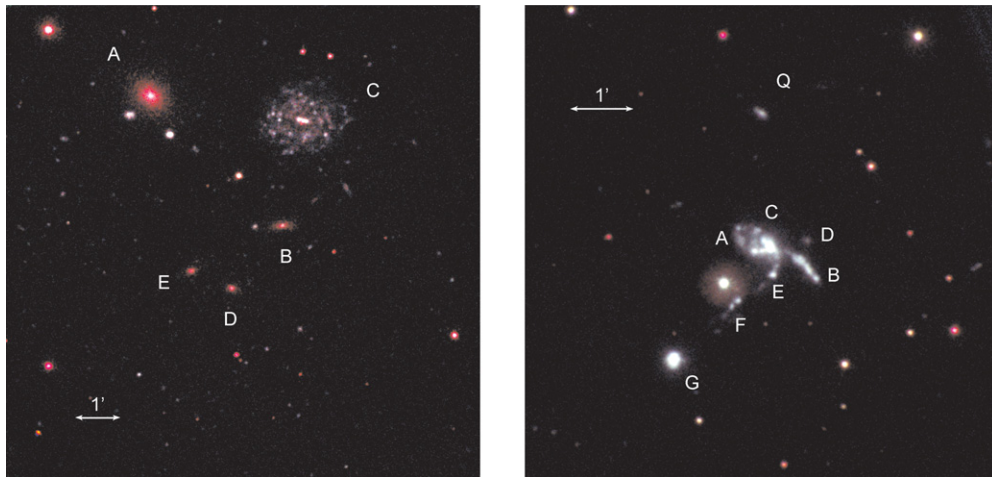(A color version of this figure is available in the online journal.)

Figure 3. *Swift*/UVOT color images as in Figure 1. Left: HCG 22. D and E are background objects. Right: HCG 31. D is a background object.
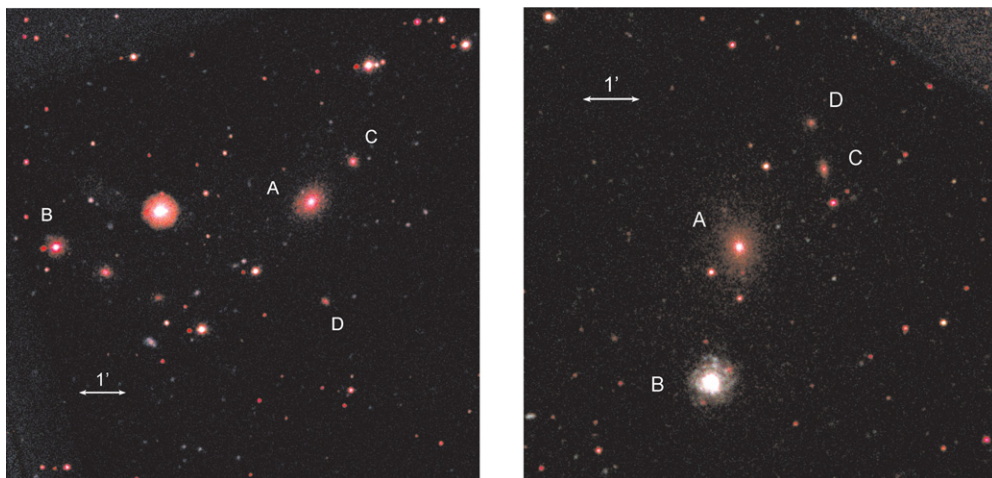(A color version of this figure is available in the online journal.)

Figure 4. *Swift*/UVOT color images as in Figure 1. Left: HCG 42. Right: HCG 48.
(A color version of this figure is available in the online journal.)

2.6. Coincidence Loss

UVOT is a photon counting detector. It thus suffers from coincidence loss at high photon rates, when two or more photons arrive at a similar location on the detector within the same CCD read out interval.[9] Since we use UVOT to make quantitative

---

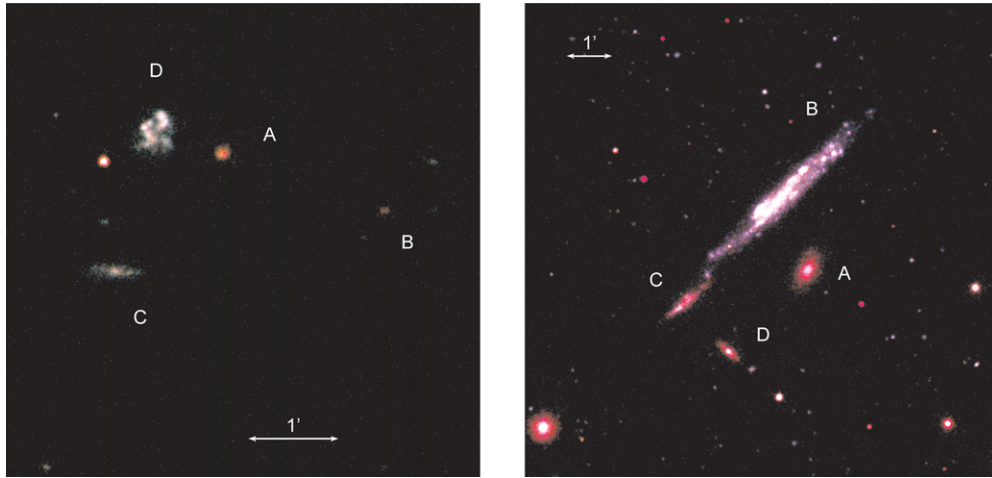[9] In X-ray work, the term *pile-up* is commonly used for this effect.

Figure 5. *Swift*/UVOT color images as in Figure 1. Left: HCG 59. Right: HCG 61. B is a foreground object.
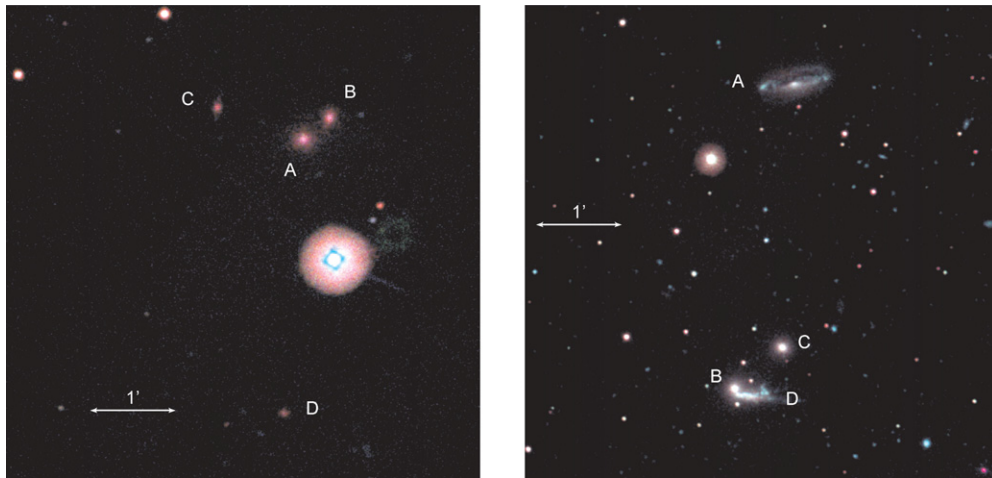(A color version of this figure is available in the online journal.)

Figure 6. *Swift*/UVOT color images as in Figure 1. Left: HCG 62. Right: HCG 90.
(A color version of this figure is available in the online journal.)

estimates, we investigate coincidence loss in the UVOT filters in greater detail. Poole et al. (2008) have calculated coincidence loss corrections in 5″ radius circular apertures for point sources (see their Figure 6) by comparing theoretical and observed count rates. They find that coincidence losses start to become important at ~ 10 counts s^{-1}. At this count-rate level, the true flux is estimated to be 5% higher. Guided by this result, we identified UV surface brightness peaks for all galaxies in our sample and obtained total, non-background subtracted count rates in all filters within such circular regions centered at the surface brightness peaks.[10]

The results of this investigation for our sample are shown in Table 6. This table aims to provide an estimate of the possible importance of coincidence loss in the ultraviolet UVOT filters for specific galaxies in our sample. We only present count rates for those circular regions that either exceed 10 counts s^{-1} or have between 5 and 10 counts s^{-1}, for the three UV filters. Among all 5″ circular source regions, there are 21, 4, 1, and 4 sources with total count rates higher than 10 counts s^{-1} in the u, $uvw1$, $uvm2$, and $uvw2$ filters, respectively. The u filter has

the highest count-rate values (up to ~ 90 counts s^{-1}), and thus clearly suffers from coincidence loss. In contrast, the shortest UV filter, $uvw2$, which is most relevant to our science results, is only modestly affected, and only for very few sources. For these sources such a result is not surprising, as these are found in some of the most UV-bright galaxies and H I-rich groups, with high levels of star formation. For instance, the highest count-rate level (~ 23 counts s^{-1}) in this filter is found at the center of the A–C merging galaxy complex in the highly disturbed central region of HCG 31. This complex, classified as an H II region, is the most luminous in our sample. However, this is an exceptional case in this filter. The other three high-count-rate sources in $uvw2$ are all very close to ~ 10 counts s^{-1}, and we consider these borderline-importance cases. Regarding the range $5 < $ counts s$^{-1} \leqslant 10$ there are 10, 2, 3, and 2 sources for the u, $uvw1$, $uvm2$, and $uvw2$ filters, respectively. The two sources in $uvw2$ are both at ~ 6 counts s^{-1}.

To summarize, coincidence loss probably only moderately affects a few bright sources in our sample. In the $uvw2$ filter, it most likely only affects one source. This may have a minor effect on our quantitative results; our qualitative results remain completely unaffected (see Section 3.2.2).

---

[10] We stress that these regions are *different* from the ones used to obtain total count rates for individual galaxies (Section 2.4).

Table 4
Ultraviolet and Infrared Flux Densities for Accordant HCG Galaxies

HCG ID	UVOT			GALEX		2MASS	MIPS
	$uvw2$[a] 2030 Å (mJy)	$uvm2$ 2231 Å (mJy)	$uvw1$ 2634 Å (mJy)	FUV 1528 Å (mJy)	NUV 2271 Å (mJy)	K_s 2.17 μm[b] (mJy)	24 μm[b] (mJy)
02a	3.894 ± 0.152^S	4.185 ± 0.141	4.203 ± 0.170	2.839 ± 0.274	3.927 ± 0.371	24.7 ± 2.5	115.0 ± 11.5
02b	1.613 ± 0.067^S	1.889 ± 0.070	1.772 ± 0.077	1.112 ± 0.111	1.832 ± 0.176	20.9 ± 2.1	351.0 ± 35.1
02c	0.984 ± 0.043^S	1.036 ± 0.042	0.991 ± 0.045	0.740 ± 0.075	0.996 ± 0.097	12.7 ± 1.3	21.5 ± 2.1
07a	0.885 ± 0.037^S	0.935 ± 0.036	1.714 ± 0.071	0.506 ± 0.051	0.883 ± 0.087	130.0 ± 13.0	303.0 ± 30.3
07b	0.258 ± 0.013^E	0.250 ± 0.013	0.736 ± 0.033	0.135 ± 0.015	0.292 ± 0.031	68.8 ± 6.9	12.7 ± 1.3
07c	2.113 ± 0.083^S	2.248 ± 0.076	2.513 ± 0.101	1.588 ± 0.155	2.212 ± 0.210	54.9 ± 5.5	76.0 ± 7.6
07d	0.632 ± 0.027^S	0.682 ± 0.028	0.876 ± 0.039	0.480 ± 0.049	0.662 ± 0.066	29.7 ± 3.0	12.0 ± 1.2
16a	1.769 ± 0.070^S	1.993 ± 0.069	2.917 ± 0.118	...	...	159.0 ± 15.9	409.0 ± 40.9
16b	0.238 ± 0.012^S	0.237 ± 0.013	0.560 ± 0.027	...	...	91.8 ± 9.2	22.5 ± 2.2
16c	2.358 ± 0.092^S	2.621 ± 0.088	3.254 ± 0.130	...	...	82.9 ± 8.3	1412.0 ± 141.2
16d	0.374 ± 0.017^S	0.389 ± 0.019	0.830 ± 0.037	...	...	72.0 ± 7.2	1785.0 ± 178.5
19a	0.156 ± 0.010^E	0.143 ± 0.011	0.400 ± 0.021	...	...	40.6 ± 4.1	3.3 ± 1.6
19b	0.338 ± 0.017^S	0.349 ± 0.018	0.374 ± 0.020	...	...	11.8 ± 1.2	24.1 ± 2.4
19c	0.550 ± 0.025^S	0.570 ± 0.026	0.520 ± 0.025	...	...	5.1 ± 1.0	6.4 ± 1.3
22a	1.386 ± 0.057^E	1.128 ± 0.045	2.635 ± 0.108	0.814 ± 0.084	1.018 ± 0.102	297.0 ± 29.7	13.9 ± 1.4
22b	0.125 ± 0.009^S	0.120 ± 0.011	0.218 ± 0.013	0.092 ± 0.012	0.139 ± 0.016	20.5 ± 2.1	1.1 ± 0.6
22c	1.532 ± 0.063^S	1.603 ± 0.060	1.525 ± 0.065	1.203 ± 0.122	1.315 ± 0.128	20.5 ± 2.1	29.4 ± 2.9
31ace	7.212 ± 0.301^S	8.000 ± 0.254	6.955 ± 0.274	6.164 ± 0.593	7.407 ± 0.690	21.3 ± 2.1	463.0 ± 46.3
31b	1.219 ± 0.064^S	1.342 ± 0.052	1.058 ± 0.048	1.018 ± 0.105	1.330 ± 0.127	3.5 ± 1.8	16.6 ± 1.7
31f	0.373 ± 0.026^S	0.514 ± 0.026	0.731 ± 0.036	0.226 ± 0.027	0.277 ± 0.031	...	2.8 ± 1.4
31g	2.388 ± 0.112^S	2.618 ± 0.092	1.905 ± 0.081	2.370 ± 0.234	2.526 ± 0.237	7.9 ± 1.6	38.9 ± 3.9
31q	0.121 ± 0.013^S	0.131 ± 0.011	0.083 ± 0.007	0.136 ± 0.017	0.169 ± 0.017	0.9 ± 0.9	0.7 ± 0.7
42a	0.999 ± 0.042^E	0.848 ± 0.036	2.663 ± 0.110	0.335 ± 0.038	0.835 ± 0.085	372.0 ± 37.2	25.5 ± 2.5
42b	0.167 ± 0.010^E	0.137 ± 0.011	0.408 ± 0.022	0.040 ± 0.007	0.157 ± 0.018	46.6 ± 4.7	4.5 ± 2.2
42c	0.204 ± 0.012^E	0.205 ± 0.014	0.587 ± 0.029	0.087 ± 0.013	0.213 ± 0.025	55.4 ± 5.5	2.8 ± 1.4
42d	0.023 ± 0.004^E	0.023 ± 0.006	0.056 ± 0.006	0.005 ± 0.002	0.039 ± 0.005	8.1 ± 1.6	0.4 ± 0.4
48a	0.868 ± 0.037^E	0.681 ± 0.031	2.316 ± 0.096	...	...	263.7 ± 26.4	12.8 ± 1.3
48b	2.054 ± 0.082^S	2.297 ± 0.081	2.551 ± 0.105	...	...	37.7 ± 3.8	81.9 ± 8.2
48c	0.054 ± 0.006^S	0.040 ± 0.008	0.149 ± 0.011	...	...	18.6 ± 1.9	0.8 ± 0.8
48d	0.033 ± 0.005^E	0.026 ± 0.007	0.081 ± 0.007	...	...	8.1 ± 1.6	0.4 ± 0.4
59a	0.177 ± 0.011^S	0.176 ± 0.013	0.345 ± 0.019	...	...	19.4 ± 1.9	453.0 ± 45.3
59b	0.037 ± 0.005^E	0.044 ± 0.007	0.076 ± 0.007	...	...	10.2 ± 1.0	0.6 ± 0.6
59c	0.212 ± 0.012^S	0.230 ± 0.015	0.192 ± 0.013	...	...	3.0 ± 1.5	3.6 ± 1.8
59d	0.870 ± 0.038^S	0.942 ± 0.041	0.831 ± 0.039	...	...	3.4 ± 1.7	12.7 ± 1.3
61a	0.980 ± 0.044^S	0.654 ± 0.029	1.100 ± 0.048	...	...	145.0 ± 14.5	20.5 ± 2.0
61c	0.944 ± 0.042^S	0.689 ± 0.031	0.818 ± 0.037	...	...	90.4 ± 9.0	357.0 ± 35.7
61d	0.312 ± 0.017^E	0.247 ± 0.015	0.351 ± 0.018	...	...	33.3 ± 3.3	2.5 ± 1.2
62a	0.508 ± 0.024^E	0.410 ± 0.021	1.816 ± 0.079	...	...	155.0 ± 15.5	9.4 ± 1.9
62b	0.137 ± 0.010^E	0.176 ± 0.013	0.670 ± 0.038	...	...	63.5 ± 6.4	3.6 ± 1.8
62c	0.128 ± 0.010^E	0.196 ± 0.014	0.459 ± 0.035	...	...	27.9 ± 2.8	2.1 ± 1.1
62d	0.018 ± 0.004^E	0.022 ± 0.006	0.065 ± 0.007	...	...	7.9 ± 1.6	1.9 ± 0.9

Notes. Flux densities are calculated from measured count rates by application of the flux conversion factors given in Table 5.
[a] Flux densities in this column have been obtained after multiplying original flux densities in the $uvw2$ filter by a factor α to compensate for the filter's red tail (see Section 2.7). Accordingly, entries are flagged either "S" ($\alpha = 0.8$) or "E" ($\alpha = 0.5$).
[b] Data from J07.

2.7. uvw2 Red Leak

Another concern with the $uvw2$ filter is the very shallow slope of the filter response function toward longer wavelengths, which in the case of very red sources can potentially lead to significant contamination of the UV flux with emission from longer wavelengths ("red leak"; Roming et al. 2009).[11] In order to investigate the effect of this red tail on different types of galaxies, we folded the full $uvw2$ effective area (response function, A_{eff}) curve, as well as modified effective area curves, $A_{eff,r}$, with galaxy templates for different morphological types. We used the publicly available templates produced with the chemical evolution code GRAZIL (Silva et al. 1998). These

models (three spirals [Sa, Sb, Sc] and one elliptical) include the effects of dust and provide good fits to local galaxy spectral energy distributions (SEDs). The $uvw2$ central wavelength, λ_c, defined as the midpoint between the FWHM wavelengths, is at 1928 Å (Poole et al. 2008). To modify the area curve redward of λ_c, we need to impose an artificial cutoff wavelength, λ_r, to A_{eff} redward of the central wavelength, so that $A_{eff,r}$ represents a new effective area curve, corresponding to a modified filter $uvw2'$. Since the A_{eff} starting wavelength is at about $\lambda_c - 1 \times$ FWHM, by symmetry, one obvious choice is $\lambda_r = \lambda_c + 1 \times$ FWHM $\simeq 2260$ Å.

In Figure 8, we illustrate how the integrated flux in a truncated $uvw2'$ filter changes for several λ_r values. Specifically, we show the trend of the ratio of the integrated fluxes in $uvw2'$ and

---

[11] This is also an issue with the $uvw1$ filter.

Table 5
Ultraviolet Count-Rate-to-Flux Conversion Factors

Filter	Conversion Factor (erg cm^{-2} Å^{-1})	rms (erg cm^{-2} Å^{-1})
	UVOT[a]	
u	1.63×10^{-16}	2.5×10^{-18}
uvw1	4.00×10^{-16}	9.7×10^{-18}
uvm2	8.50×10^{-16}	5.6×10^{-18}
uvw2	6.2×10^{-16}	1.4×10^{-17}
	GALEX[b]	
NUV	2.06×10^{-16}	. . . [c]
FUV	1.40×10^{-15}	. . . [c]

Notes.
[a] Data taken from Poole et al. (2008), Table 10.
[b] http://galexgi.gsfc.nasa.gov/docs/galex/FAQ/counts_background.html.
[c] No data available.
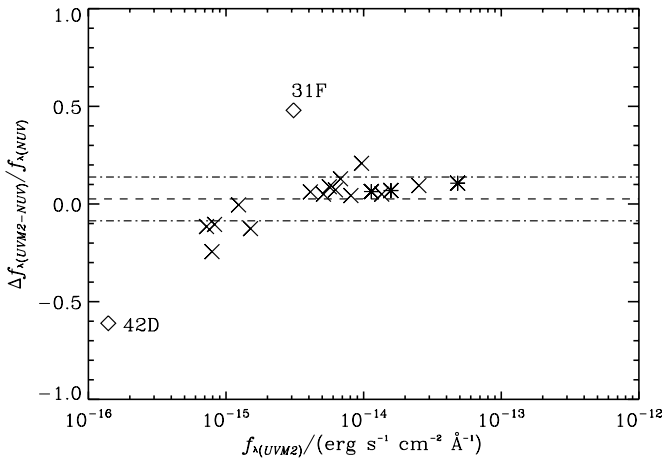
Figure 7. Fractional difference in flux between the UVOT *uvm2* and *GALEX* NUV filters for HCG galaxies observed with both *GALEX* and *Swift*. The two extreme outliers, HCG 31 F and HCG 42 D, are indicated by diamonds. The three sources which may be subject to some coincidence loss in the *uvm2* filter are shown by asterisks and are HCGs 2 B, 31 G, and 31 ACE in order of increasing *uvm2* flux. The dashed line indicates the mean fractional difference calculated from a subset of the points, excluding the two outliers. The dash-dotted lines indicate the standard deviation on the mean result.

uvw2 as a function of λ_r. With $\lambda_r = 2260$ Å, the artificially "narrowed" filter contains ∼0.5 of the flux in the full filter for the elliptical template and ∼0.8 for the spiral templates. Conversely, this implies that ∼0.5 (0.2) of the flux in the original, full filter is due to emission redward of 2260 Å for the elliptical template (spiral templates). Even if the cutoff is moved 200 Å further toward the red, the difference in flux between full and narrowed filter is significant, with filter-flux ratios of ∼0.6 and ∼0.9 for the two main morphological classifications. These results will likely vary depending on the particular SEDs of real galaxies, reflecting a variety of star formation history and dust content. However, similar trends can be observed with different templates, e.g., Bruzual & Charlot (2003), and so in order to minimize contamination of UV flux by non-UV emission from the red tail, we impose a cutoff at 2260 Å. This cutoff assumes that, in reality, only a fraction, α, of the calculated flux density in the *uvw2* filter comes from the UV wavelength region. For the assumed cutoff, $\alpha = 0.5$ for E/S0 galaxies and 0.8 otherwise. Although this choice directly affects SFR estimates, the quantitative effect is small; qualitatively our results remain entirely unaffected (see Section 3.2.2 for details).

Table 6
Importance of Coincidence Loss in UVOT HCG Data

HCG[a]	uvw1 (counts s^{-1})	uvm2 (counts s^{-1})	uvw2 (counts s^{-1})
		>10 counts s^{-1}	
2 B	12.33	⩽10	10.43
16 C	16.46	⩽10	12.85
31 ACE	22.6	15.17	23.40
31 G	11.57	⩽10	11.70
		$5 < $ counts s$^{-1} \leqslant 10$	
2 A	6.74	⩽5	5.84
2 B	⩽5	6.70	⩽5
16 A	9.38	⩽5	5.85
16 C	⩽5	8.71	⩽5
31 G	⩽5	7.47	⩽5

Notes. Total count rates are grouped for sources with >10 counts s^{-1} (top) and those with $5 <$ counts s$^{-1} \leqslant 10$ (bottom) in the three ultraviolet *Swift* UVOT filters. Upper limit entries imply a source has a count rate lower than the lower limit of its tabulated group (less than either 10 or 5 counts s^{-1}).
[a] Column gives the HCG galaxy for which the total count rate in a 5″-radius circular aperture centered on an emission peak is shown in the adjacent columns with no background subtracted.
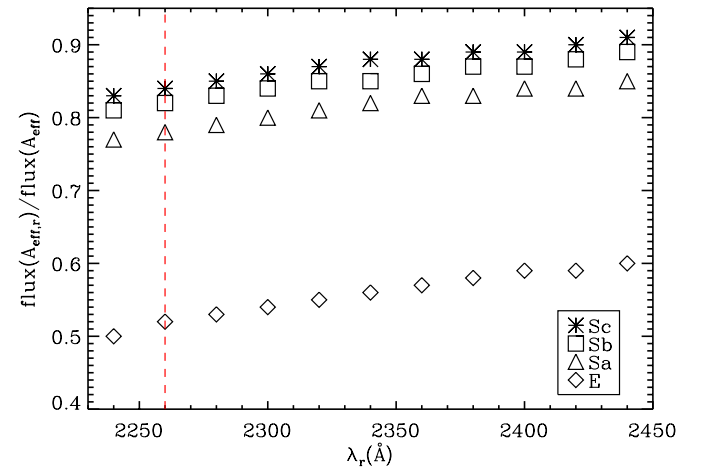

Figure 8. Illustration of effect of imposing an artificial cutoff to the *uvw2* filter. The original full-filter effective area, $A_{\rm eff}$, is modified by a cutoff at λ_r, so that the new effective area is $A_{\rm eff,r}$. The original and modified filters are folded with model templates for different galaxy types (Silva et al. 1998), shown in the legend, and the corresponding fluxes are calculated. The ratios of these fluxes are plotted as a function of the imposed cutoff wavelength. For all galaxy types, it is clear that there is a significant difference between the flux level in the full filter and that in the narrowed filter, i.e., there is significant contribution from emission captured by the filter's red tail which does not originate in the UV wavelength region. Thus, as explained in the text, for the purpose of calculations in this paper, a fraction of the total filter flux corresponding to the estimated red tail contribution is excluded. The adopted value for the cutoff wavelength is shown by the dashed line.
(A color version of this figure is available in the online journal.)

2.8. Comparison Sample

For the purposes of comparison, we use the *Spitzer* Infrared Nearby Galaxy Survey (SINGS; Kennicutt et al. 2003) to construct a comparison subsample. As in G08, we select galaxies which have $\log L_{\nu,J} = 27.70$–30.17 (erg s^{-1} Hz^{-1}), in order to better match the HCG sample luminosity range. The HCG sample comprises mostly 3–5 bright galaxies per group, and this selection filters mostly low-luminosity SINGS dwarfs. In addition, we use the non-interacting ("normal") SINGS catalog
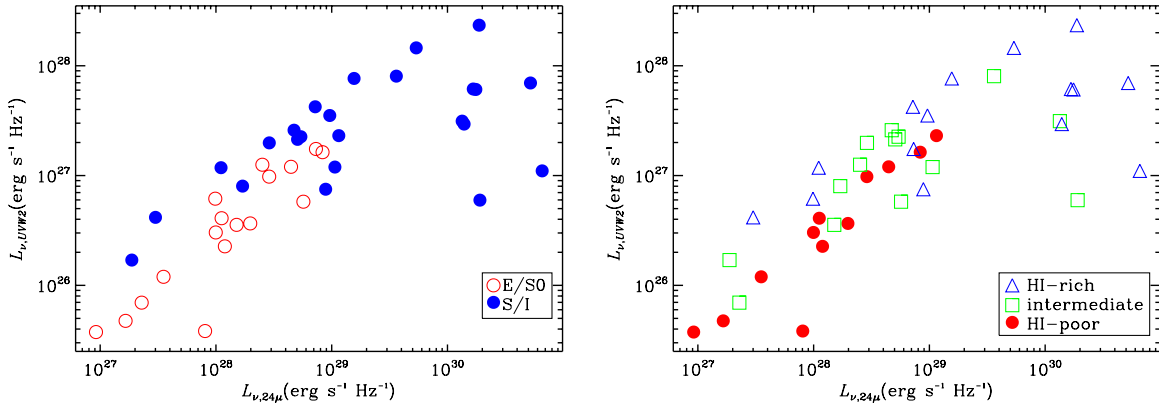
Figure 9. $L_{\nu,uvw2}$ vs. $L_{\nu,24\,\mu m}$ for HCG galaxies. Left: E/S0's (S/I's) are shown with open (filled) circles. Right: for each galaxy, parent-group gas richness is indicated with triangles (rich), squares (intermediate), and filled circles (poor). There is a good correlation of $uvw2$ and 24 μm luminosity up to log L_ν(24 μm) $\sim$30.
(A color version of this figure is available in the online journal.)

of Smith et al. (2007a, their Table 2) to remove galaxies for which there is evidence that they are strongly interacting. According to Smith et al. (2007a), target galaxies are deemed interacting if "they have companions whose velocities differ from that of the target galaxy by $\leqslant$1000 km s^{-1}, that have an optical luminosity brighter than 0.1 of the target galaxy, and are separated from the target galaxy by less than 10 times the optical diameter of the target galaxy or the companion, whichever is larger." These criteria still allow for some of these galaxies to have distant or low-mass companions but, as Smith et al. (2007a) note, they are guaranteed to be less perturbed than the Milky Way. This additional selection is in fact warranted by a clear effect on the final subsample: it leads to the elimination of all SINGS galaxies which have some level of peculiarity (their morphological designation includes "p"). We thus obtain a SINGS control subsample of 33 galaxies which in the broadest sense are similar to our HCG galaxies (due to the $L_{\nu,J}$ matching) but are otherwise in relatively quiescent environments. Although a few of these galaxies are members of the Virgo galaxy cluster, they still fulfill the non-interaction and isolation criteria, and we do not exclude them from the comparison sample. We use the photometry in Tables 2 and 3 of Dale et al. (2007) to calculate the same parameters as for the HCG galaxies.

3. RESULTS

3.1. UV and IR Comparisons

In Figure 9, we plot monochromatic luminosities, L_ν, in the $uvw2$ and 24 μm bands for individual galaxies in the 11 HCGs of our sample. In this and following plots, we use different symbols to separate galaxies according to morphological type (either E/S0 or S/I) and parent-group H I-gas content (rich—type I, intermediate—type II, poor—type III). $uvw2$ luminosity correlates with 24 μm luminosity up to log L_ν(24 μm) $\sim$30 where a turn-over and/or larger scatter dominate. This is likely the effect of higher dust attenuation at higher luminosities and SFRs (Hopkins et al. 2001; Buat et al. 2007). E/S0 galaxies and gas-poor groups tend to be less luminous than S/I galaxies and gas-rich groups both in the $uvw2$ and in the 24 μm band. This luminosity segregation appears to be somewhat more pronounced when galaxies are classified by morphological type than it is when galaxies are classified by parent-group gas richness. We show later that this behavior characterizes other star formation related properties as well. The broad UV–IR correlation persists over $\sim$3 dex in luminosity for both wavelength
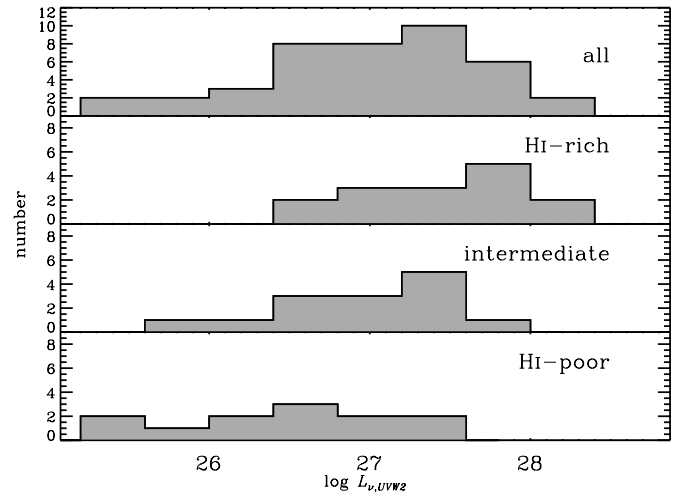

Figure 10. $uvw2$ monochromatic luminosity distribution for HCG galaxies. Distributions are shown for the full sample, as well as subsamples according to group H I content. Group H I richness appears to correlate with $L_{\nu,uvw2}$.

bands, indicative, on average, of a consistent contribution from the UV.

In Figure 10, we plot the distribution of $uvw2$ luminosity for the full HCG sample, as well as subsamples based on parent-group H I richness. Overall, $L_{\nu,uvw2}$ appears to correlate with H I richness, in the sense that galaxies brightest in $L_{\nu,uvw2}$ tend to belong to more gas-rich groups. This *trend* of the distributions by group H I type is broadly the same as in the equivalent plot for the 24 μm data (J07, Figure 14). This is consistent with the general correlation between the $uvw2$ and 24 μm luminosities.

In Figure 11, we show the ratio of power in the 24 μm and $uvw2$ bands, $\nu L_{\nu,24\,\mu m}/\nu L_{\nu,uvw2}$, as a function of Hubble type. This ratio only takes into account one UV and one IR band, so it is not an adequate quantitative estimate of the overall relative contributions from the UV and the IR. Additionally, it suffers from small number statistics. However, at least qualitatively, there are some notable patterns. For 33 out of the full sample of 41 HCG galaxies ($\sim$80%) $\nu L_{\nu,24\,\mu m}/\nu L_{\nu,uvw2} \leqslant 1$, i.e., the contribution to the total energy budget from power emerging at 2000 Å is at least as important as that at 24 μm. Only eight galaxies emit more power in the 24 μm band than they do at 2000 Å. Among these only one is an elliptical, with the rest being spirals or irregulars. For ellipticals, the generally low values of
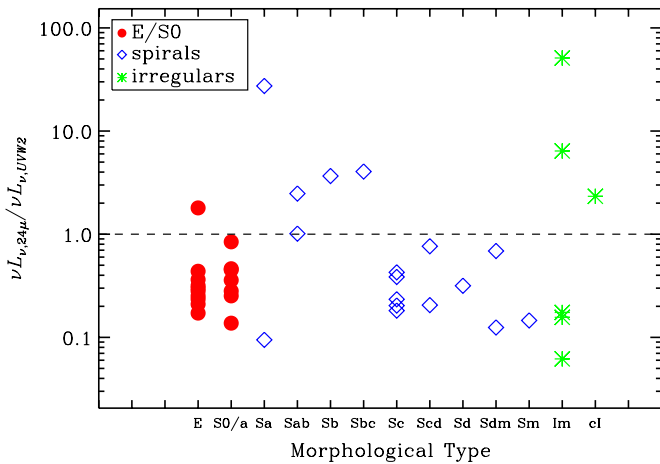
Figure 11. Ratio of 24 μm-to-*uvw2* power, $\nu L_{\nu,24\,\mu m}/\nu L_{\nu,uvw2}$, vs. galaxy optical morphology. The horizontal dashed line marks the locus of equal contributions from 24 μm and *uvw2* power. There is a significant contribution from the *uvw2* band.

(A color version of this figure is available in the online journal.)

the $\nu L_{\nu,24\,\mu m}/\nu L_{\nu,uvw2}$ ratios likely reflect the lower levels of star formation and associated dust production. The trend for spirals seems to be different. With the exception of HCG 22 B (a type Sa at $\nu L_{\nu,24\,\mu m}/\nu L_{\nu,uvw2} \sim 0.1$), the 24 μm contribution is highest for the earlier types (Sa's), getting progressively lower for later types. As spirals are actively star forming, high dust levels and associated 24 μm emission are expected. However, the UV contribution from the most actively star-forming later types seems to be more than compensating for the presence of dust. Finally, irregulars show a large range in values. This is mainly due to the presence of galaxies HCG 16 C, D, the two type Im systems with the highest values of $\nu L_{\nu,24\,\mu m}/\nu L_{\nu,uvw2}$. Both galaxies have high SFRs ($\sim$14 and 17 $M_\odot$ yr^{-1}; Table 7), and are likely recent merger remnants, with highly disturbed velocity fields and double nuclei (Mendes de Oliveira et al. 1998).

3.2. Star Formation Rates

3.2.1. Method

One of the most important properties characterizing a galaxy is the rate at which it forms stars. Active star formation is traced directly or indirectly by young stellar populations (10^6–10^8 yr) whose light is dominated by O and early B stars. UV continuum emission (1250–2500 Å), as well as Hα line emission, from massive stars provides a direct probe of these populations. However, a significant part of this light is often heavily absorbed by dust and re-emitted in the IR wavelength region (1–1000 μm). UV-based SFR calibrations (e.g., Kennicutt 1998; Salim et al. 2007) thus require a correction for intrinsic extinction, to avoid significant underestimates of the true SFR. Conversely, IR-based calibrations (e.g., Calzetti et al. 2007; Rieke et al. 2009) adopt the "dusty starburst approximation,"by assuming that the bulk of the UV emission is re-emitted in the IR (also known as the "calorimeter assumption").

Thus, in general the total SFR contains both a dust-obscured component, which can be measured from the IR, and an unobscured component, measured directly from the UV (Bell et al. 2003; Hirashita et al. 2003; Iglesias-Páramo et al. 2006; Dale et al. 2007). In this paper, we obtain the two components independently using calibrations from the literature. In particular,

we use

$$\mathrm{SFR_{TOTAL}} \equiv \mathrm{SFR_{UV+IR}} \equiv \mathrm{SFR}_{UVW2} + \mathrm{SFR}_{24\,\mu m}, \quad (1)$$

where

$$\mathrm{SFR}_{uvw2}(M_\odot\ \mathrm{yr}^{-1}) = 9.5 \times 10^{-44}\ \nu L_{\nu,uvw2}\ (\mathrm{erg\ s}^{-1}) \quad (2)$$

and

$$\mathrm{SFR}_{24\,\mu m}(M_\odot\ \mathrm{yr}^{-1}) = 2.14 \times 10^{-42}\ \nu L_{\nu,24\,\mu m}\ (\mathrm{erg\ s}^{-1})\ . \quad (3)$$

Equation (2) estimates SFR$_{\mathrm{UV}}$ from the *uvw2* luminosity using the calibration by Kennicutt (1998), valid for a Salpeter initial mass function (IMF) and continuous star formation over $\lesssim 10^8$ yr. *uvw2* luminosity probes the spectral region around $\sim$2000 Å, which is the approximate center of the spectrally flat UV wavelength range, 1500–2800 Å. It thus provides a "mean" estimate of UV emission properties (Hirashita et al. 2003; Kennicutt 1998).

Equation (3) uses the 24 μm luminosity and the Rieke et al. (2009, hereafter R09) calibration (their Equation (10)) to estimate SFR$_{\mathrm{IR}}$. This is based on the calorimeter assumption and is most appropriate for 24 μm luminosities $>10^{42.36}$ erg s^{-1}. At lower luminosities, significant numbers of UV photons escape and need to be accounted for. Most of our galaxies fall in this regime, and we account directly for non-negligible UV emission. In essence, we use SFR$_{24\,\mu m}$ to obtain an effective extinction correction for SFR$_{uvw2}$. Uncertainties related to the use of these calibrations are addressed in Section 4.2.2.

Whereas SFRs provide an absolute measure of current star-forming activity in a galaxy, SSFRs relate this to the products of past star formation (Guzman et al. 1997; Brinchmann & Ellis 2000; Feulner et al. 2005). SSFR is defined as

$$\mathrm{SSFR} \equiv \frac{\mathrm{SFR}}{M_*}, \quad (4)$$

where M_* is the galaxy total stellar mass. In general, star-forming galaxies are still actively increasing M_* and have not yet reached their maximum values. We expect the situation to be reversed for gas-poor galaxies dominated by old stellar populations. Thus, this normalization can help distinguish galaxies according to their star formation history. We use K_s-band luminosities as a proxy for M_*, and normalize SFRs calculated via Equation (1), assuming $M_*/M_\odot = 0.8\ \nu\ L_{\nu,K_s}/L_\odot$ (Bell et al. 2003).

3.2.2. Results

Total and SSFR results for our HCG galaxies are tabulated in Table 7. For each galaxy, we also give galaxy morphology, nuclear classification, parent-group H I richness, UVOT ultraviolet and MIPS 24 μm luminosities, stellar masses, the ratio of SFR$_{\mathrm{UV}}$ to SFR$_{\mathrm{TOTAL}}$, as well as α_{IRAC} values.

Introduced by G08, α_{IRAC} is an MIR activity index. It is evaluated by means of a power-law fit to the 4.5, 5.7, and 8 μm data ($L_\nu \propto \nu^{\alpha_{\mathrm{IRAC}}}$). The 3.6 μm band has been excluded as it is dominated by the Rayleigh–Jeans tail of stellar photospheres. The MIR regime hosts several emission features from polycyclic aromatic hydrocarbon (PAH) molecules, which are vibrationally excited upon absorption of single UV/optical photons (Leger & Puget 1984; Allamandola et al. 1985). Among the three bands used for the fit, the 4.5 μm is the one least affected by PAH emission (Draine & Li 2007), while the 8 μm is the one most

Table 7
UV and IR Properties Of HCG Galaxies

HCG ID (1)	Galaxy Morphology[a] (2)	Nuclear Type[b] (3)	Group H I Type[a] (4)	$\log L_\nu$ (erg s^{-1} Hz^{-1})[c] uvw2 (5)	uvm2 (6)	uvw1 (7)	$24\,\mu$m (8)	M_*[d] ($10^9\,M_\odot$) (9)	$\alpha_{\rm IRAC}$[e] (10)	SFR[f] ($M_\odot$ yr^{-1}) (11)	$\frac{\mathrm{SFR}_{uvw2}}{\mathrm{SFR}_{\rm TOTAL}}$ [g] (12)	SSFR[h] (10^{-11} yr^{-1}) (13)
Actively Star Forming												
2a	SBd	R	I	28.16	28.29	28.29	29.73	3.32	-2.89 ± 0.03	3.418 ± 0.276	0.60	102.89 ± 16.31
2b	cI	R	I	27.79	27.95	27.93	30.22	2.86	-3.76 ± 0.18	5.153 ± 0.589	0.17	179.95 ± 31.97
2c	SBc	?	I	27.55	27.67	27.65	28.98	1.64	-2.35 ± 0.36	0.741 ± 0.060	0.67	45.27 ± 7.23
7a	Sb	H II	II	27.50	27.62	27.88	30.13	16.6	-2.23 ± 0.09	3.882 ± 0.468	0.11	23.46 ± 4.25
7c	SBc	?	II	27.91	28.03	28.08	29.56	7.52	-2.53 ± 0.58	2.056 ± 0.169	0.55	27.33 ± 4.34
7d	SBc	?	II	27.33	27.46	27.57	28.70	3.61	-1.69 ± 0.29	0.429 ± 0.035	0.70	11.89 ± 1.90
16a	SBab	LINER, X, R	I	27.78	27.93	28.10	30.25	19.68	-2.85 ± 0.26	5.371 ± 0.621	0.16	27.29 ± 4.87
16c	Im	SBNG	I	27.84	27.99	28.08	30.72	8.81	-4.39 ± 0.46	14.378 ± 1.827	0.07	163.12 ± 30.39
16d	Im	LINER	I	27.04	27.16	27.49	30.82	7.64	-3.79 ± 0.07	17.062 ± 2.313	0.01	223.34 ± 43.01
19b	Scd	?	II	27.08	27.19	27.22	29.03	1.50	-2.96 ± 0.30	0.441 ± 0.041	0.38	29.37 ± 4.85
19c	Sdm	ELG	II	27.30	27.41	27.37	28.46	0.66	-1.90 ± 0.61	0.352 ± 0.033	0.79	53.13 ± 12.51
22c	SBcd	ELG	II	27.35	27.47	27.45	28.73	1.09	-1.55 ± 0.14	0.455 ± 0.040	0.69	41.88 ± 7.04
31ace	Sdm	H II	I	28.37	28.51	28.45	30.27	2.49	-3.51 ± 0.05	8.107 ± 0.737	0.40	325.78 ± 53.05
31b	Sm	H II	I	27.63	27.77	27.66	28.86	0.44	-2.07 ± 0.86	0.777 ± 0.068	0.76	177.78 ± 94.20
31f	Im	?	I	27.07	27.31	27.46	28.04	...	...	0.194 ± 0.024	0.85	...
31g	Im	?	I	27.88	28.02	27.88	29.19	0.91	-2.15 ± 0.30	1.474 ± 0.122	0.73	161.56 ± 38.28
31q	Im	?	I	26.62	26.75	26.55	27.48	0.11	-0.95 ± 0.45	0.066 ± 0.011	0.88	59.34 ± 60.44
48b	Sc	X	III	27.36	27.51	27.55	29.06	1.53	-2.80 ± 0.41	0.619 ± 0.055	0.52	40.59 ± 6.79
59a	Sa	?	II	26.78	26.87	27.16	30.28	2.35	-2.42 ± 0.46	4.985 ± 0.665	0.02	212.01 ± 40.11
59c	Sc	?	II	26.90	27.03	26.96	28.23	0.41	-2.00 ± 0.48	0.156 ± 0.025	0.72	38.24 ± 20.41
59d	Im	?	II	27.41	27.54	27.49	28.67	0.36	-2.34 ± 0.32	0.484 ± 0.041	0.75	132.84 ± 68.46
61c	Sbc	AGN, R	I	27.47	27.43	27.50	30.14	10.15	-3.23 ± 0.09	3.990 ± 0.486	0.10	39.32 ± 7.14
Quiescent												
7b	SB0	?	II	26.76	27.05	27.52	28.76	8.88	1.14 ± 0.18	0.227 ± 0.022	0.36	2.56 ± 0.42
16b	Sab	Sy2	I	26.88	26.97	27.34	28.95	10.42	0.12 ± 0.30	0.333 ± 0.033	0.32	3.20 ± 0.54
19a	E2	ABS	II	26.55	26.81	27.26	28.18	5.34	1.36 ± 0.21	0.089 ± 0.020	0.56	1.66 ± 0.44
22a	E2	dSy2	II	27.10	27.31	27.68	28.40	15.49	1.40 ± 0.22	0.240 ± 0.020	0.73	1.55 ± 0.25
22b	Sa	ABS	II	26.23	26.31	26.57	27.27	1.01	1.47 ± 0.41	0.029 ± 0.004	0.83	2.84 ± 0.54
42a	E3	dLINER, X	III	27.21	27.44	27.94	28.92	35.00	1.78 ± 0.18	0.443 ± 0.037	0.52	1.26 ± 0.20
42b	SB0	ABS	III	26.56	26.78	27.25	28.30	5.90	1.42 ± 0.50	0.102 ± 0.026	0.50	1.73 ± 0.51
42c	E2	ABS	III	26.61	26.91	27.37	28.05	6.38	1.68 ± 0.09	0.086 ± 0.016	0.67	1.35 ± 0.31
42d	E2	ABS	III	25.68	25.98	26.36	27.22	0.97	1.69 ± 0.47	0.011 ± 0.004	0.61	1.13 ± 0.52
48a	E2	ABS	III	26.99	27.19	27.72	28.46	17.10	1.26 ± 0.30	0.211 ± 0.018	0.65	1.23 ± 0.20
48c	S0a	?	III	26.08	26.24	26.82	27.55	2.36	1.51 ± 0.06	0.026 ± 0.009	0.65	1.09 ± 0.43
48d	E1	?	III	25.57	25.77	26.27	26.96	0.54	1.67 ± 0.42	0.008 ± 0.003	0.69	1.42 ± 0.59
59b	E0	?	II	25.84	26.22	26.46	27.36	1.12	1.65 ± 0.19	0.016 ± 0.006	0.62	1.40 ± 0.58
61a	S0a	Sy2, R	I	27.24	27.37	27.59	28.86	14.88	0.82 ± 0.50	0.432 ± 0.036	0.57	2.91 ± 0.46
61d	S0	ABS	I	26.79	26.99	27.14	27.99	3.78	1.24 ± 0.48	0.112 ± 0.016	0.77	2.95 ± 0.58
62a	E3	dLINER, X	III	27.08	27.29	27.93	28.65	21.13	1.29 ± 0.11	0.283 ± 0.031	0.60	1.34 ± 0.23
62b	S0	ABS, X	III	26.36	26.77	27.35	28.08	6.06	1.31 ± 0.22	0.062 ± 0.016	0.51	1.03 ± 0.30
62c	S0	ABS	III	26.48	26.97	27.34	28.00	3.81	1.51 ± 0.54	0.068 ± 0.014	0.62	1.79 ± 0.44
62d	E2	ABS	III	25.58	25.96	26.44	27.91	0.96	1.49 ± 0.00	0.026 ± 0.011	0.21	2.70 ± 1.26

Notes. Galaxies with $\alpha_{\rm IRAC} \leqslant 0$ and high SSFR are presented separately ("actively star forming," upper table) from those with $\alpha_{\rm IRAC} > 0$ and low SSFR ("quiescent," lower table). These two groups of galaxies show a pronounced bimodality in $\alpha_{\rm IRAC}$ and SSFR, as explained in the text.
[a] As in Table 1.
[b] Same as G08, Table 3. ABS: absorption-line galaxy; AGN: active galactic nucleus; (d)Sy2: (dwarf) Seyfert 2; X: X-ray source; R: radio source; (d)LINER: (dwarf) low-ionization nuclear emission region; SBNG: starburst nucleated galaxy; H II: strong H II emitter; ELG: emission-line galaxy; "?": unknown.
[c] Logarithm of monochromatic luminosities for the three ultraviolet *Swift* UVOT filters and the *Spitzer* MIPS $24\,\mu$m filter.
[d] Total stellar mass estimated from 2MASS K_s-band luminosity assuming $M_*/M_\odot = 0.8\,\nu\,L_{\nu,K_s}/L_\odot$ (Bell et al. 2003).
[e] MIR activity index calculated from power-law fit, $L_\nu \propto \nu^{\alpha_{\rm IRAC}}$ to 4.5–8 μm *Spitzer* IRAC luminosities.
[f] Total SFR estimated using Equation (1).
[g] Fraction of SFR$_{\rm TOTAL}$ due to *uvw2* (2000 Å) emission.
[h] SSFR calculated by normalizing SFR$_{\rm TOTAL}$ by M_* (Column 11 divided by Column 9).

affected. Thus, if there is significant PAH emission, $\alpha_{\rm IRAC}$ will be negative (MIR SED decreasing with ν). Additionally, the MIR includes a thermal continuum component ("hot dust") attributed to very small grains (Li & Draine 2001; Draine &

Li 2007). $\alpha_{\rm IRAC}$ will also be negative if this component is strong.

G08 detected a significant gap, with no $\alpha_{\rm IRAC}$ values between -0.95 and 0.12. As the origin of negative $\alpha_{\rm IRAC}$ values is

Table 8
Sings Comparison Subsample Galaxies in the SSFR Gap

SINGS ID	Galaxy Morphology	M_* ($10^9\,M_\odot$)	α_{IRAC}	SFR ($M_\odot\,\mathrm{yr}^{-1}$)	SSFR ($10^{-11}\,\mathrm{yr}^{-1}$)	Comments
(1)	(2)	(3)	(4)	(5)	(6)	(7)
NGC 1291	SB0/a	12.74	1.22	0.450	3.53	HIPASS J0317-41[a]
NGC 4450	SAab	14.88	0.33	0.700	4.70	[b]
NGC 2841	SAb	8.83	−0.82	0.640	7.25	[c]
NGC 4579	SABb	25.08	−0.62	2.040	8.13	[c,b]
NGC 4826	SAab	5.70	−0.74	0.530	9.29	[c,d]
NGC 4725	SABab	24.27	−1.00	2.360	9.72	

Notes. Galaxies are from the SINGS subsample obtained by selecting SINGS galaxies that (1) have luminosities which fall within the luminosity range for HCG galaxies and (2) appear to be non-interacting and isolated (see Section 2.8 for details). Morphology information (RC3) is taken from Dale et al. (2007). The rest of the data are derived as in Table 7 based on Dale et al. (2007).
[a] Koribalski et al. 2004.
[b] Virgo cluster galaxies.
[c] Also in α_{IRAC} gap.
[d] Evidence of counter-rotating gaseous disk (Braun et al. 1992).
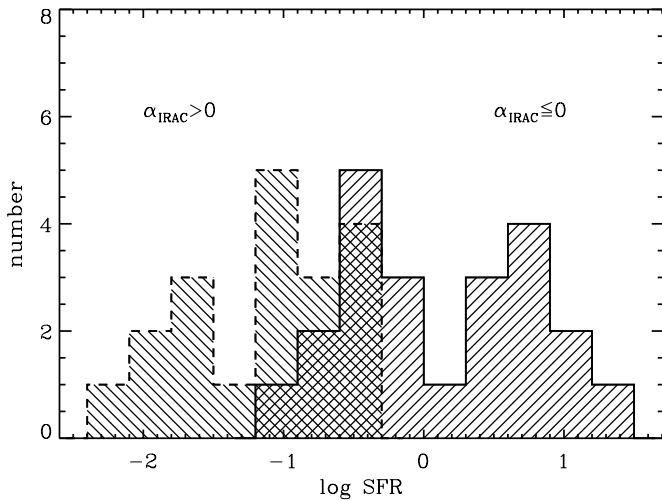
Figure 12. SFR distributions for the two HCG subsamples of MIR-active ($\alpha_{\mathrm{IRAC}} \leqslant 0$) and $\alpha_{\mathrm{IRAC}} > 0$ (MIR quiescent) galaxies. The total distribution is continuous.
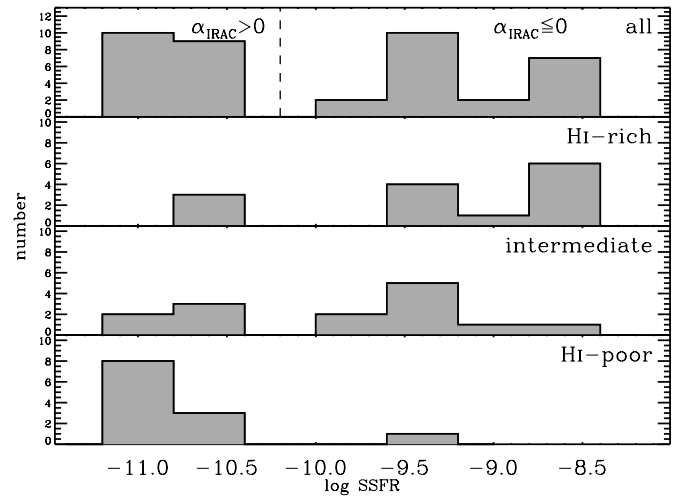

Figure 13. SSFR distributions for HCG galaxies. Top: full sample. The dashed vertical line marks the gap between the high-SSFR (right) and the low-SSFR (left) part of the distribution. All galaxies to the right of this gap have $\alpha_{\mathrm{IRAC}} \leqslant 0$ (MIR active). All galaxies to the left of the gap have $\alpha_{\mathrm{IRAC}} > 0$ (MIR quiescent). The bimodality is clear (compare to Figure 12). Bottom three panels: subsamples of galaxies belonging to HCGs of decreasing gas richness, as labeled. SSFR values appear to correlate with H I-gas richness.

ultimately star-forming and/or AGN activity, they label galaxies with $\alpha_{\mathrm{IRAC}} \leqslant 0$ as MIR active, and those with $\alpha_{\mathrm{IRAC}} > 0$ as MIR quiescent.

In Figure 12, we show the SFR distributions for MIR-active and MIR-quiescent galaxies in the same panel. On average, MIR-active galaxies have higher SFRs than MIR-quiescent ones, but, taken as a whole, the distribution for the full galaxy sample presents a continuous aspect. However, this picture changes when SSFRs, the distributions for which are shown in Figure 13, are considered. Here, SSFR distributions for the total sample are shown in the top panel. Distributions for subsamples, defined according to group gas richness, are shown in the three lower panels. The SSFR distribution for the full sample shows a clear bimodality. High-SSFR galaxies ($1.2 \times 10^{-10} \lesssim$ SSFR/yr$^{-1} \lesssim 5 \times 10^{-9}$) are separated from low-SSFR ones ($1 \times 10^{-11} \lesssim$ SSFR/yr$^{-1} \lesssim 3.2 \times 10^{-11}$) by a gap of magnitude $\sim 9 \times 10^{-11}$ yr^{-1}. A two-sided Kolmogorov–Smirnov test gives a probability $\sim 4 \times 10^{-9}$ for the low-SSFR and high-SSFR distributions to come from the same parent population. Further, this bimodality coincides completely with the bimodality in the α_{IRAC} index: all low-SSFR galaxies have $\alpha_{\mathrm{IRAC}} > 0$ (and vice versa), and similarly for high-SSFR galaxies and $\alpha_{\mathrm{IRAC}} \leqslant 0$.

On the other hand, the subsample distributions indicate that gas-rich groups preferentially contain high-SSFR galaxies, groups of intermediate gas richness have a broad distribution of SSFRs, covering almost the full range of SSFR values, and gas-poor groups show a pronounced peak in low SSFRs.

We plot α_{IRAC} against SSFR in Figure 14. In the left-hand panel, we use different symbols to denote E/S0 and S/I morphological types. For comparison, galaxies from the SINGS control subsample are also shown. Several patterns are apparent here. First, the bimodality in SSFR is not shared by the SINGS-subsample galaxies, similarly to the case of the bimodality in α_{IRAC}, also exclusive to HCG galaxies (G08). A two-sided Kolmogorov–Smirnov test gives a probability $\sim 1.3 \times 10^{-3}$ for the SINGS-subsample and HCG-full-sample SSFR distributions to come from the same parent population. The six SINGS galaxies that populate the SSFR gap are shown in Table 8. One is a lenticular and the rest are spirals of relatively early
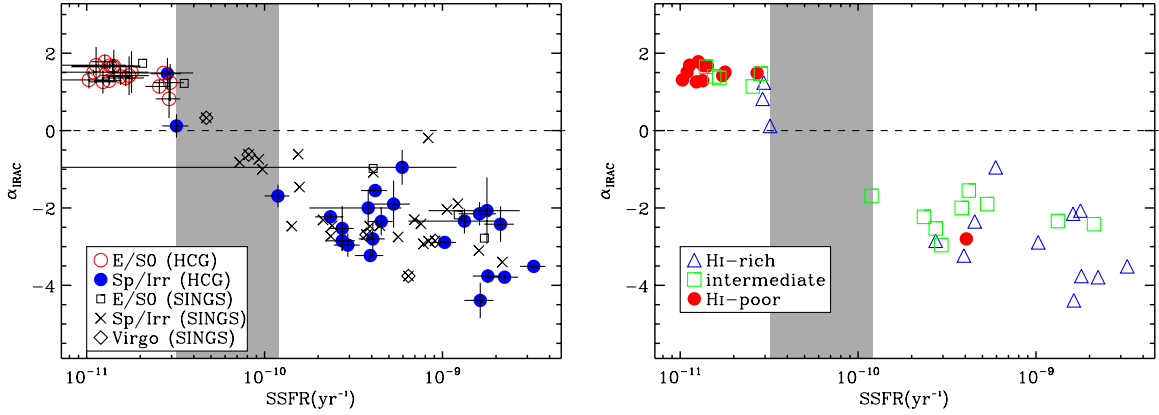
Figure 14. α_{IRAC} MIR activity index vs. SSFR. The horizontal dashed line indicates the α_{IRAC} gap. The SSFR gap is shown as a shaded region. Error bars are only shown in the left-hand plot. Left: plotting symbols indicate morphological types, as shown in the legend, for both HCG and SINGS-subsample galaxies. In addition, diamonds indicate SINGS galaxies which are members of the Virgo cluster. All SINGS galaxies have been selected to match the luminosity range for HCG galaxies, as well as to be isolated and non-interacting. The large error bar for the point at SSFR $\sim 6 \times 10^{-10}$ yr^{-1} is due to the fact that this (HCG 31 Q) is the faintest galaxy in the K_s band with a 100% fractional error in flux density. The SSFR gap for HCG galaxies almost completely separates quiescent E/S0 galaxies from actively star-forming S/I types, and is populated by some SINGS-subsample galaxies. Right: plotting symbols indicate parent-group H I-gas richness for HCG galaxies as shown in the legend. The SSFR gap for HCG galaxies in general appears to separate H I-rich from H I-poor groups.

(A color version of this figure is available in the online journal.)

type. The mean K-band derived stellar mass for these galaxies is $1.5 \times 10^{10}\,M_\odot$. For higher SSFR SINGS galaxies outside the gap this value is 5.7×10^9. All galaxies are classified as low-ionization nuclear emission region (LINER) or low-luminosity AGN (LLAGN) from the MIR analysis of Smith et al. (2007b). Given the small numbers and the fact that 10/25 (40%) of the SINGS-subsample galaxies outside the gap, as well as many HCG galaxies, are also LINER/LLAGN, this is not significant. It is likely that these are largely isolated galaxies, which have accumulated significant stellar mass and are on their way to becoming quiescent ellipticals.

Second, in the HCG sample, with the exception of two galaxies, the $\alpha_{IRAC} > 0$/low-SSFR and $\alpha_{IRAC} \leqslant 0$/high-SSFR regions are populated exclusively by E/S0's and S/I's, respectively. In this respect, SINGS galaxies do not differ: the lower SSFR systems are E/S0 and the great majority of high-SSFR systems are S/I. The three E/S0 systems with high SSFR are NGC 0855, which is possibly an edge-on spiral misclassified as E/S0 (Phillips et al. 1996), NGC 3773, a high-SFR dwarf irregular in the process of becoming a dwarf elliptical (Dellenbusch et al. 2008), and NGC 1377, which, in spite of its optical morphology, is a "nascent starburst" (Roussel et al. 2006).

The right-hand panel in Figure 14 shows HCG galaxies with symbols indicating parent-group H I richness. Comparing with the left-hand panel, we note that the general correspondence between, on the one hand, S/I morphology and high gas richness, and, on the other hand, E/S0 morphology and low gas richness is evident, as noted already by J07 and G08. However, the morphological segregation is somewhat more pronounced than the segregation according to parent-group H I-gas content, as was the case when comparing $L_{\nu,uvw2}$ to $L_{\nu,24\,\mu m}$. Morphologically, there are only two S/I galaxies—an Sa and an Sab—at the high-SSFR edge of the low-SSFR group (Figure 14, left). In contrast, in Figure 14 (right), there is a gas-poor group galaxy (HCG 48 B) in the high-SSFR locus, while intermediate group-richness galaxies cover a broad range of both the low and high-SSFR regimes.

It is important to stress that the SSFR bimodality and gap are only detected when scaling by total stellar mass. It is also

only present when a total (UV+IR) SFR is calculated. The distributions of L_{ν,K_s}, SFR$_{UV}$, and SFR$_{24\,\mu m}$, are not bimodal and none of them alone can give rise to the SSFR bimodality. In contrast, the bimodality can be traced to genuine *absolute* SFR differences, evident in Figure 12 which are enhanced by the normalization by total stellar mass.

Two final points are in order regarding these results. First, the comparison with the SINGS-subsample shows that there is no pronounced difference in the *level* of activity between HCG and (luminosity-matched, non-interacting) SINGS galaxies. On the whole, HCGs show neither significantly higher nor significantly lower SFRs. Second, we note that the effect of the *uvw2* filter cutoff imposed (or, equivalently, the exclusion of a fraction of the measured *uvw2* flux) with the aim of correcting for the effects of the filter's red tail (Section 2.7) is minimal. If we impose no cutoff whatsoever, and so calculate all results using the full flux in the *uvw2* filter, almost all SFR values increase by less than 0.3 $M_\odot$ yr^{-1}. The only two exceptions are HCGs 31 ACE and 2 A, which increase by 0.8 and 0.5 $M_\odot$ yr^{-1}, respectively. The SSFR gap remains prominent and, although slightly shifted to higher values, its width remains essentially the same at 8.7×10^{-11} yr^{-1} (versus 8.8×10^{-11} yr^{-1}). All qualitative results are completely unaffected. Similar remarks apply to the effects of coincidence losses. The effect is small, and, in any case, all galaxies that may be affected (Table 6) belong to the high-SFR group. Hence, if coincidence losses were to be taken into account, we would expect these galaxies to show even higher SFRs and SSFRs.

4. DISCUSSION

4.1. The Evolution of Hickson Compact Groups

J07 were the first to detect a gap in MIR color space, separating galaxies in gas-rich groups from those in gas-poor groups. G08 found further evidence for a separation between these two classes of HCG galaxies in the form of a gap in α_{IRAC} values. The SSFR estimates in the present paper support and extend these results. Our results show that S/I galaxies
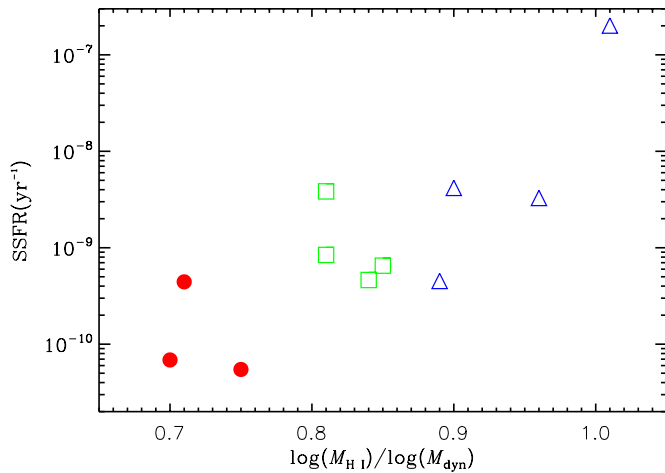
Figure 15. Total group SSFR vs. log $M_{\rm H\,I}$/log $M_{\rm dyn}$ for each galaxy group in our sample. Plotting symbols indicate parent-group H I-gas richness as in Figure 14. There is a broad trend for H I-richer groups to have higher SSFRs.

(A color version of this figure is available in the online journal.)

Figure 16. SSFR vs. morphological type for individual galaxies in our HCG sample. Plotting symbols indicate parent-group H I-gas richness as in Figure 14. For a given galaxy type, galaxies in groups with higher H I-gas richness tend to have higher SSFRs.

(A color version of this figure is available in the online journal.)

in our sample populate preferentially groups that are gas rich (type I) or of intermediate gas richness (type II), have high SSFRs, and are MIR active. E/S0 galaxies are seen to populate mostly groups that are gas poor (type III) or type II, have low SSFRs, and are MIR inactive. Thus, S/I and E/S0 HCG galaxies may constitute two distinct subclasses, consistent with being the two extremes of a possible evolutionary sequence progressing from the S/I—high-SSFR subclass to the E/S0—low-SSFR one. The overall amount of H I-gas in the group appears to correlate with this bimodality. Intermediate H I-richness groups play an important role within the context of such an evolutionary scheme. They contain all morphological types and cover the full range of observed SSFRs (Figure 13). This might suggest that they are representative of the environment where the morphological transformation is most actively under way. Evidence for a progression from H I-rich groups to H I-poor groups is also seen at the *group* scale. In Figure 15, we plot the *total* group SSFR against the corresponding total group log $M_{\rm H\,I}$/log $M_{\rm dyn}$ ratio. The broad correlation observed (Spearman $\rho = 0.75$ for a probability 8×10^{-3} that the variables are uncorrelated) suggests that SSFR broadly tracks the depletion of the gas supply. Figure 16 shows that for a given morphology, galaxies in H I-rich groups have higher SSFR than galaxies in H I-intermediate and poor groups. Note though that it is possible for much of the H I-gas to be outside the galaxies where most of the star formation may be taking place. As we lack high-resolution H I data for all of our sample galaxies at the present time, we are unable to investigate this point any further.

This simple picture is useful only as a first approximation, in which H I richness is a proxy for evolutionary stage. As can be seen in Figure 14 (right panel) and Table 7, there are three galaxies belonging to H I-rich groups at the *low* end of the SSFR gap. Two of these (61 A and B) are type S0 and S0a, and the third (16b) Sab. For such systems, H I richness does not tell the whole story. In reality, an evolutionary scheme should include several criteria. Column 7 in Table 1 is a qualitative estimate of evolutionary stage, using galaxy morphologies and the presence or absence of an X-ray bright IGM. According to this, the parent groups of these galaxies are in late and intermediate stages, consistent with their SSFR.

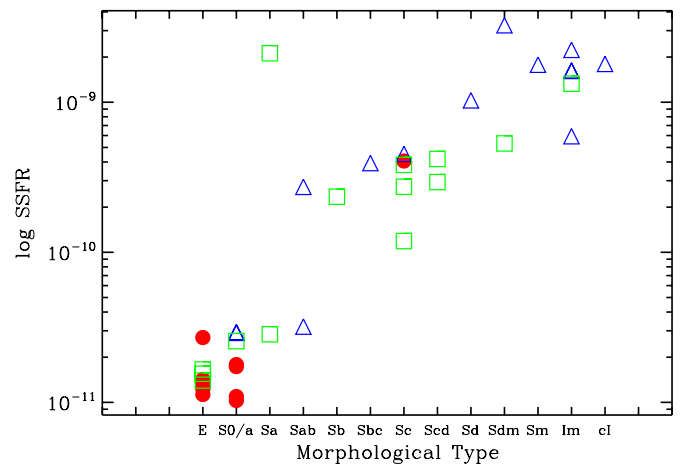Thus, HCG evolution needs to be examined on a case-by-case basis. In some cases, a group may be H I poor perhaps

mainly because gas has been used up by member galaxies to fuel rapid star formation. In other cases, gas-stripping under the effect of violent interactions, will end star formation in the member galaxies, but the group may still be relatively gas rich. A complete picture requires studying both individual galaxies and all phases of the group IGM. Although in this paper we focus exclusively on the bright HCG galaxies, it has been shown that in a number of cases, star formation takes place outside of galaxies, as a result of tidal stripping of H I gas from individual galaxies (de Mello et al. 2008; Torres-Flores et al. 2009). Such evidence provides a complementary viewpoint for HCG evolution. Indeed, the evolutionary scheme proposed by Verdes-Montenegro et al. (2001) takes into account H I *distribution* as well as H I deficiency. Future work (L. M. Walker et al. 2010, in preparation) will be using high-resolution H I data to explore the links between H I content, H I distribution, SSFR, and $\alpha_{\rm IRAC}$.

In any case, the existence of significant gaps in both $\alpha_{\rm IRAC}$ and SSFR suggests that this evolution is rapid. This must be linked to the special environment of HCGs. No such gaps are found in the SINGS comparison subsample. It must be noted that the original, full SINGS sample was designed to include a range in galaxy properties, and so does not favor the detection of a SSFR gap. However, from the full SINGS sample we have selected those galaxies that match the HCG galaxy-luminosity range and appear to be isolated and non-interacting. Otherwise, this SINGS subsample shows the same range in properties such as morphologies, stellar masses, and absolute range of SFRs and SSFRs as the HCG sample. What appears to be different is the distribution of SFRs and SSFRs, which, unlike in HCGs, appears to be continuous. The general level of star formation also appears to be consistent with that in other environments. In the Verdes-Montenegro et al. (1998) HCG sample, FIR and H_2 emission in HCG galaxies is comparable to that in isolated, Virgo cluster as well as weakly interacting systems.

Walker et al. (2009) compare MIR color distributions for the JG sample to a set of diverse environments, including core and infall regions of the Coma cluster, interacting galaxies, as well the combined Local Volume Legacy (Dale et al. 2009) and SINGS samples. They find evidence for another gap in MIR color space in the Coma cluster "infall" region. No gaps are found in any of the other environments. This is further evidence

that a high-density, low velocity dispersion environment clearly plays a key role in accelerating star formation processes.

Finally, a note regarding the evolutionary hypothesis. In this paper, we present several lines of evidence for an evolutionary sequence from gas-rich groups, mostly containing S/I galaxies, to gas-poor groups, mostly containing E/S0 systems. However, there is no independent evidence excluding the possibility that observed gas-rich groups with S/I galaxies are *not* the direct precursors of observed gas-poor groups with E/S0 systems. In other words, it is still possible that gas-poor and gas-rich groups are two distinct classes of CGs. The characteristics of intermediate gas-richness groups mitigate this possibility but it cannot be excluded altogether.

4.2. Caveats

4.2.1. The Origin of UV Emission

In interpreting our SFR results, we are making two simplifying assumptions. The first is that UV emission traces exclusively active star formation, i.e., emission from young, massive stars. In reality, low-mass He-burning stars which undergo a post-asymptotic giant branch (AGB) phase also emit in the UV. In star-forming galaxies, this emission will make up for a small fraction of the total UV emission, which is dominated by massive OB stars. However, in quiescent galaxies (E/S0) this is not necessarily the case. Such stars are known to be responsible for a "UV excess" (UVX) or "UV upturn," sometimes observed in such systems (Dorman et al. 1995; O'Connell 1999). However, it is only shortward of $\lesssim 2000$ Å that UV elliptical-galaxy SEDs are starting to become affected by the UV upturn. As the *uvw2* effective wavelength is at 2030 Å, it is possible that the integrated flux from this filter will at least not be dominated by any UV upturn in ellipticals. Further, UV emission from ellipticals can indeed be due to residual star formation. This is well known for at least a number of nearby systems (O'Connell 1999). Usually these are galaxies that have undergone recent interactions or mergers. The HCG environment is similarly highly interaction prone. Verdes-Montenegro et al. (1998) detect CO emission in a number of HCG ellipticals. This signifies the existence of significant reservoirs of cold gas in these systems which they attribute to the recent merger of a gas-rich companion. In the HCG environment, gas transfer, either via mergers between gas-rich and gas-poor galaxies or via continuous infall from the IGM, can well be an ongoing process that fuels star formation. Given that the evidence suggests a rapid morphological evolution for HCG galaxies, it would not be surprising that ellipticals show signs of some ongoing star formation. In any case, correcting for the UV emission from old stars will reduce the true SFR and SSFR values at the low end of the observed SSFR gap, so that this will be even larger.

Our second assumption is that we may neglect any AGN contribution to the *uvw2* and 24 μm emission used to obtain SFR estimates. This is reasonable for our sample which contains no known Seyfert-1 types. Coziol et al. (1998) also find that as much as 50% of AGN detected in their HCG sample are faint LLAGN, either Seyfert-2 or LINERs, hidden by a strong stellar continuum. In our sample, the majority of known AGNs are classified as Seyfert-2 or LINER (Table 7, Column 3). There are a few such cases among both actively star-forming and quiescent HCG galaxies (top and bottom part of Table 7, respectively). In the case of star-forming galaxies, these are not likely to dominate emission at UV or IR wavelengths. In the case of quiescent galaxies, an AGN contribution would lead to an overestimate of

emission due to low-level star formation. All of our quiescent galaxies have $\alpha_{\rm IRAC} > 0$, suggesting reduced contributions from PAH emission and hot dust in the MIR band. MIR quiescence has been associated with the presence of LLAGN (Roche et al. 1991; Smith et al. 2007b). However, as in the case of contribution to the UV emission from old stars, correcting for this effect would lead to reduced SFR and SSFR values, making the observed SSFR gap larger.

4.2.2. SFR Estimates

The errors for SFR and SSFR values presented in Table 7 reflect uncertainties in the *uvw2* and 24 μm photometry and flux conversion factors. In addition, the *uvw2* to SFR$_{\rm UV}$ calibration (Equation (2)) includes an uncertainty of at least 0.3 dex in the calculated SFR$_{\rm UV}$, depending on which stellar population synthesis models are used for deriving it (Kennicutt 1998).

The 24 μm to SFR$_{\rm IR}$ calibration is most appropriate for 24 μm bright galaxies. According to the estimates of R09, for galaxies with $\nu \, L_{\nu, 24\,\mu m} > 10^{42.36}$ erg s^{-1}, this calibration includes a small correction (2.5%) for UV photons not re-emitted in the IR, which are thus detectable in the UV. Some of our brightest galaxies fall in this luminosity regime, so there is a possibility that SFR$_{\rm TOTAL}$ may be overestimated for these systems. However, the actual level of UV leakage for specific galaxies is difficult to assess, as it depends as much on luminosity as it does on geometry. This correction is also within the 10% uncertainty margin introduced by the conversion of 24 μm luminosity to total IR luminosity (R09, Equations (4) and (5)). We thus attempt no further corrections for this effect.

Further, the R09 calibration uses an IMF which leads to SFR$_{24\,\mu m}$ values ~ 0.66 times those obtained with a standard Salpeter IMF, assumed by Kennicutt's SFR$_{\rm UV}$ formula. The choice of the most appropriate IMF is not a settled issue, and, given the wide use of the Salpeter IMF, we choose to use the R09 24 μm calibration together with the Kennicutt (1998) 2000 Å calibration, with no further modifications, in spite of the IMF discrepancy. We have tested that, if the R09 calibration is adjusted so that this disagreement disappears, on average SFR$_{\rm TOTAL}$ values increase by $\sim 0.7 \, M_\odot$ yr^{-1}, and SSFR values by 17×10^{-11} yr^{-1}. The SSFR gap undergoes a slight increase in width to 9.4×10^{-11} yr^{-1}.

4.2.3. HCG Triplets

As already mentioned, there are claims that HCGs with only three accordant members may need to be treated separately. We have checked that this issue is irrelevant for the present paper. There are four triplets in our sample, containing 12 out of the total 41 galaxies. However, these appear to be randomly distributed in $\alpha_{\rm IRAC}$, SFR, and SSFR space, so that excluding them leaves the main results of this paper completely unaffected. In particular, there is no change in the magnitude both of the $\alpha_{\rm IRAC}$ and of the SSFR gap.

4.2.4. H I Richness

There is no particular physical reason for the $\log M_{\rm H I}/ \log M_{\rm dyn}$ boundaries selected to classify HCGs into H I-richness types (Section 2.1). These boundaries were chosen arbitrarily by J07, to obtain roughly equal numbers of galaxies in each richness category. A different choice would lead to somewhat different versions for all of our figures which show galaxies according to parent-group H I richness, but the overall picture does not change. Additionally, our definition of group H I richness does

not explicitly take into account member galaxy morphology. This is particularly problematic for groups which have no S/I galaxies, but there are only two such groups in our sample. However, in spite of this arbitrariness, it is clear from Figures 15 and 16 that H I richness, as defined here, does track star formation activity and gas depletion.

5. SUMMARY AND FUTURE PROSPECTS

We have presented the UV data for 41 galaxies from the JG HCG bright-galaxy sample. We combined *Swift* UVOT *uvw2* (2000 Å) photometry and *Spitzer* MIPS 24 μm photometry to obtain SFR and SSFR estimates.

The following are the main results of this paper.

1. $L_{\nu, uvw2}$ and $L_{\nu, 24\,\mu m}$ are significantly correlated up to $L_{\nu, 24\,\mu m} \sim 10^{30}$ erg s^{-1} Hz^{-1}, where dust extinction of UV emission becomes important.
2. When SFRs are normalized by stellar mass to calculate SSFRs, the HCG galaxies have a clear bimodal distribution that indicates galaxies are either actively star forming (SSFR $\gtrsim 1.2 \times 10^{-10}$ yr^{-1}) or almost entirely quiescent ($\lesssim 3.2 \times 10^{-11}$ yr^{-1}). From previous work, the index α_{IRAC}, a measure of the strength of dust emission from 4.5–8 μm, is also known to be strongly bimodal. SSFR correlates significantly with α_{IRAC} for the HCG galaxies, i.e., the galaxies with the reddest MIR SEDs have the highest SSFR.
3. The bimodality in SSFR is mirrored closely by galaxy morphology. All elliptical/S0 galaxies have low SSFR values, and 22 out of 24 spiral/irregular galaxies have high SSFR values.
4. The bimodality in SSFR is also mirrored by the H I-gas richness of a galaxy's parent group. Twelve out of 15 galaxies belonging to groups with high levels of H I-gas have high SSFR values, and 11 out of 12 galaxies belonging to groups with little H I-gas have low SSFR values. Galaxies in HCGs with intermediate amounts of H I gas span almost the entire range of calculated SSFR values.
5. When compared to a subsample of SINGS galaxies selected to be non-interacting, isolated and to match HCG galaxies in near-IR luminosity, HCG galaxies have the same range of SFRs and SSFRs. However, the SINGS subsample galaxies do not demonstrate the same bimodality in either α_{IRAC} or SSFR. This difference is interpreted as a consequence of the CG environment accelerating galaxy evolution by enhancing star formation and leading to rapid gas depletion, followed by a quick transition to quiescence.

In the near future, better understanding of the HCG environment will come by combining information from several wavelength regions.

A major step is to obtain broadband galaxy SEDs ranging from the UV to the IR. We have completed a ground-based imaging campaign with the aim of carrying out multi-filter (*B*, *V*, *R*, *I*) photometry for the JG sample. We have also complete NIR wide-field imaging with WIRCam at the Canada–France–Hawaii telescope.

The *Swift*, *Spitzer*, WIRCam, and ground-based photometry provides coverage from $\sim$2000 Å to 24 μm. SED fitting will provide independent and more complete estimates of SFRs, SSFRs, and dust attenuation. UV–optical photometry can also better probe the UV upturn in early-type galaxies (e.g., Schawinski et al. 2007).

From what we know at present, AGNs are not prevalent in this sample. Seven of the HCGs in our sample have been observed

with *Chandra* (PI: Gallagher, as well as archival observations), and these data will allow us to better explore this issue. At the same time, we will investigate the H I–X-ray anticorrelation via the detection (or otherwise) of diffuse X-ray emission. Further, SFRs and X-ray luminosities will also be used to investigate the X-ray–SFR correlation, which has been established in the field, but has not yet been investigated in the HCG environment.

An increase in galaxy sample size is desirable for improving statistics. We are engaged in a comprehensive optical spectroscopic campaign with the aim of detecting new, lower luminosity members of HCGs. It will be instructive to re-examine the SFR and SSFR results when more HCG member galaxies can be included.

REFERENCES

Allam, S., Assendorp, R., Longo, G., & Richter, G. 1995, Planet. Space Sci., 43, 1371
Allamandola, L. J., Tielens, A. G. G. M., & Barker, J. R. 1985, ApJ, 290, L25
Baron, E., & White, S. D. M. 1987, ApJ, 322, 585
Barton, E. J., de Carvalho, R. R., & Geller, M. J. 1998, AJ, 116, 1573
Bell, E. F., McIntosh, D. H., Katz, N., & Weinberg, M. D. 2003, ApJS, 149, 289
Braun, R., Walterbos, R. A. M., & Kennicutt, Jr., R. C. 1992, Nature, 360, 442
Brinchmann, J., & Ellis, R. S. 2000, ApJ, 536, L77
Bruzual, G., & Charlot, S. 2003, MNRAS, 344, 1000
Buat, V., et al. 2007, ApJS, 173, 404
Calzetti, D., et al. 2007, ApJ, 666, 870
Cardelli, J. A., Clayton, G. C., & Mathis, J. S. 1989, ApJ, 345, 245
Coziol, R., Ribeiro, A. L. B., de Carvalho, R. R., & Capelato, H. V. 1998, ApJ, 493, 563
Da Rocha, C., & Mendes de Oliveira, C. 2005, MNRAS, 364, 1069
Da Rocha, C., Ziegler, B. L., & Mendes de Oliveira, C. 2008, MNRAS, 388, 1433
Dale, D. A., et al. 2007, ApJ, 655, 863
Dale, D. A., et al. 2009, ApJ, 703, 517
de Carvalho, R. R., Gonçalves, T. S., Iovino, A., Kohl-Moreira, J. L., Gal, R. R., & Djorgovski, S. G. 2005, AJ, 130, 425
de Mello, D. F., Torres-Flores, S., & Mendes de Oliveira, C. 2008, AJ, 135, 319
Dellenbusch, K. E., Gallagher, III, J. S., Knezek, P. M., & Noble, A. G. 2008, AJ, 135, 326
Dole, H., et al. 2006, A&A, 451, 417
Dorman, B., O'Connell, R. W., & Rood, R. T. 1995, ApJ, 442, 105
Draine, B. T., & Li, A. 2007, ApJ, 657, 810
Feulner, G., Goranova, Y., Drory, N., Hopp, U., & Bender, R. 2005, MNRAS, 358, L1
Gallagher, S. C., Johnson, K. E., Hornschemeier, A. E., Charlton, J. C., & Hibbard, J. E. 2008, ApJ, 673, 730
Gehrels, N., et al. 2004, ApJ, 611, 1005
Geller, M. J., & Huchra, J. P. 1983, ApJS, 52, 61
Guzman, R., Gallego, J., Koo, D. C., Phillips, A. C., Lowenthal, J. D., Faber, S. M., Illingworth, G. D., & Vogt, N. P. 1997, ApJ, 489, 559
Hickson, P. 1982, ApJ, 259, 930
Hickson, P., Kindl, E., & Auman, J. R. 1989, ApJS, 70, 687
Hickson, P., Mendes de Oliveira, C., Huchra, J. P., & Palumbo, G. G. 1992, ApJ, 399, 353
Hirashita, H., Buat, V., & Inoue, A. K. 2003, A&A, 410, 83
Hopkins, A. M., Connolly, A. J., Haarsma, D. B., & Cram, L. E. 2001, AJ, 122, 288
Iglesias-Páramo, J., et al. 2006, ApJS, 164, 38
Johnson, K. E., Hibbard, J. E., Gallagher, S. C., Charlton, J. C., Hornschemeier, A. E., Jarrett, T. H., & Reines, A. E. 2007, AJ, 134, 1522

Kelm, B., & Focardi, P. 2004, A&A, 418, 937
Kennicutt, R. C. 1998, ARA&A, 36, 189
Kennicutt, Jr, R. C., et al. 2003, PASP, 115, 928
Kennicutt, R. C., et al. 2009, ApJ, 703, 1672
Koribalski, B. S., et al. 2004, AJ, 128, 16
Leger, A., & Puget, J. L. 1984, A&A, 137, L5
Li, A., & Draine, B. T. 2001, ApJ, 554, 778
Mendes de Oliveira, C., & Hickson, P. 1994, ApJ, 427, 684
Mendes de Oliveira, C., Plana, H., Amram, P., Bolte, M., & Boulesteix, J. 1998, ApJ, 507, 691
Morrissey, P., et al. 2005, ApJ, 619, L7
Mulchaey, J. S. 2000, ARA&A, 38, 289
Mulchaey, J. S., Davis, D. S., Mushotzky, R. F., & Burstein, D. 2003, ApJS, 145, 39
Nolthenius, R., & White, S. D. M. 1987, MNRAS, 225, 505
O'Connell, R. W. 1999, ARA&A, 37, 603
Phillips, A. C., Illingworth, G. D., MacKenty, J. W., & Franx, M. 1996, AJ, 111, 1566
Ponman, T. J., Bourner, P. D. J., Ebeling, H., & Böhringer, H. 1996, MNRAS, 283, 690
Poole, T. S., et al. 2008, MNRAS, 383, 627
Press, W. H., & Schechter, P. 1974, ApJ, 187, 425
Rasmussen, J., Ponman, T. J., Verdes-Montenegro, L., Yun, M. S., & Borthakur, S. 2008, MNRAS, 388, 1245
Reines, A. E., Johnson, K. E., & Goss, W. M. 2008, AJ, 135, 2222
Rieke, G. H., Alonso-Herrero, A., Weiner, B. J., Pérez-González, P. G., Blaylock, M., Donley, J. L., & Marcillac, D. 2009, ApJ, 692, 556
Roche, P. F., Aitken, D. K., Smith, C. H., & Ward, M. J. 1991, MNRAS, 248, 606
Roming, P. W. A., Gronwall, C., vanden Berk, D. E., Page, M. J., & Boyd, P. T. 2009, Ap&SS, 320, 203

Roming, P. W. A., et al. 2005, Space Sci. Rev., 120, 95
Rood, H. J., & Struble, M. F. 1994, PASP, 106, 413
Rose, J. A. 1977, ApJ, 211, 311
Roussel, H., et al. 2006, ApJ, 646, 841
Rubin, V. C., Hunter, D. A., & Ford, W. K. J. 1991, ApJS, 76, 153
Salim, S., et al. 2007, ApJS, 173, 267
Schawinski, K., et al. 2007, ApJS, 173, 512
Schlegel, D. J., Finkbeiner, D. P., & Davis, M. 1998, ApJ, 500, 525
Shimada, M., Ohyama, Y., Nishiura, S., Murayama, T., & Taniguchi, Y. 2000, AJ, 119, 2664
Silva, L., Granato, G. L., Bressan, A., & Danese, L. 1998, ApJ, 509, 103
Smith, B. J., Struck, C., Hancock, M., Appleton, P. N., Charmandaris, V., & Reach, W. T. 2007a, AJ, 133, 791
Smith, J. D. T., et al. 2007b, ApJ, 656, 770
Sulentic, J. W. 1997, ApJ, 482, 640
Sulentic, J. W. 2000, in ASP Conf. Ser. 209, IAU Colloq. 174: Small Galaxy Groups, ed. M. J. Valtonen & C. Flynn (San Francisco, CA: ASP), 226
Sulentic, J. W., Rosado, M., Dultzin-Hacyan, D., Verdes-Montenegro, L., Trinchieri, G., Xu, C., & Pietsch, W. 2001, AJ, 122, 2993
Torres-Flores, S., Mendes de Oliveira, C., de Mello, D. F., Amram, P., Plana, H., Epinat, B., & Iglesias-Páramo, J. 2009, A&A, 507, 723
Tovmassian, H. M., Martinez, O., & Tiersch, H. 1999, A&A, 348, 693
Verdes-Montenegro, L., Yun, M. S., Perea, J., del Olmo, A., & Ho, P. T. P. 1998, ApJ, 497, 89
Verdes-Montenegro, L., Yun, M. S., Williams, B. A., Huchtmeier, W. K., Del Olmo, A., & Perea, J. 2001, A&A, 377, 812
Walker, L. M., Johnson, K. E., Gallagher, S. C., Hibbard, J. E., Hornschemeier, A. E., Charlton, J. C., & Jarrett, T. H. 2009, in Proc. The Galaxy Wars: Stellar Populations and Star Formation in Interacting Galaxies, in press (arXiv:0908.2971)